

Pattern formation of quantum Kelvin-Helmholtz instability in binary superfluidsHaruya Kokubo,¹ Kenichi Kasamatsu,¹ and Hiromitsu Takeuchi²¹*Department of Physics, Kindai University, Higashi-Osaka, Osaka 577-8502, Japan*²*Department of Physics and Nambu Yoichiro Institute of Theoretical and Experimental Physics (NITEP), Osaka City University, Sumiyoshi-ku, Osaka 558-8585, Japan*

(Received 30 April 2021; accepted 30 June 2021; published 13 August 2021)

We study theoretically the nonlinear dynamics induced by shear-flow instability in segregated two-component Bose-Einstein condensates in terms of the Weber number, which is defined by extending the past theory on the Kelvin-Helmholtz instability in classical fluids. Numerical simulations of the Gross-Pitaevskii equations demonstrate that dynamics of pattern formation is well characterized by the Weber number We , clarifying the microscopic aspects unique to the quantum fluid system. For $We \lesssim 1$, the Kelvin-Helmholtz instability induces flutter-finger patterns of the interface and quantized vortices are generated at the tip of the fingers. The associated nonlinear dynamics exhibits a universal behavior with respect to We . When $We \gtrsim 1$ in which the interface thickness is larger than the wavelength of the interface mode, the nonlinear dynamics is effectively initiated by the counter-superflow instability. In a strongly segregated regime and a large relative velocity, the instability causes transient zipper pattern formation instead of generating vortices due to the lack of circulation to form a quantized vortex per a finger. In a weakly segregating regime and a small relative velocity, the instability leads to the sealskin pattern in the overlapping region, in which the frictional relaxation of the superflow cannot be explained only by the homogeneous counter-superflow instability. We discuss the details of the linear and nonlinear characteristics of this dynamical crossover from small to large Weber numbers, where microscopic properties of the interface become important for the large Weber number.

DOI: [10.1103/PhysRevA.104.023312](https://doi.org/10.1103/PhysRevA.104.023312)**I. INTRODUCTION**

Hydrodynamic instability in superfluids is one of the important topics in a research field of quantum fluids, being deeply related with a generation mechanism of quantum turbulence [1]. The Kelvin-Helmholtz instability (KHI), one of the fundamental instabilities in classical hydrodynamics, occurs when two phase-separated fluid components undergo a shear flow beyond the critical relative velocity [2,3]. The KHI in quantum fluids, referred to as quantum KHI (QKHI), has been studied in superfluid helium [4–6], atomic Bose-Einstein condensates (BECs) [7–10], and nuclear superfluids in a neutron stars [11]. A cold atomic BEC is a versatile system to study the hydrodynamic instability and the associated nonlinear dynamics because ideal configurations suitable to study the relevant problems can be prepared in a well-controlled manner; for example, a flat interface between different superfluids can be prepared by using binary BECs with tunable interatomic interactions [12–15]. The interface dynamics, the hydrodynamic instabilities, and the nonlinear dynamics in immiscible two-component BECs have been studied in some papers [16–31]. Even for the miscible case, the binary BECs exhibit the countersuperflow instability (CSI) [32], which results in a train of solitons in a one-dimensional (1D) case or the complicated turbulent structure in two-dimensional (2D) or three-dimensional (3D) systems [33–37].

The linear stability analysis of stationary flowing states in immiscible binary superfluids can be explored in the hydro-

dynamic model based on the low-energy effective action of a quantized interface excitation, i.e., a ripplon. In a previous study [7], the QKHI of a thin interface of strongly segregated binary BECs has been studied. The nonlinear stage of the evolution has shown that, just above the critical relative velocity, the initial flat interface between the two condensates deforms into sawtooth waves and generates singly quantized vortices on the peaks and troughs of the waves. The subsequent work addresses the stability analysis and resulting nonlinear dynamics with increasing the interface thickness to the miscible limit, revealing the crossover behavior from the KHI to the CSI [8].

In this work, we study theoretically the nonlinear evolution in immiscible two-component BECs with a shear flow in a wide range of system parameters. The characteristics of the nonlinear dynamics is summarized in the phase diagram parametrized by the relative velocity and the intercomponent coupling strength. We find that the comparison relation of the two important scales, namely, the wavelength of the unstable interface excitations and the thickness of the interface, determines the boundary of different regimes of nonlinear evolution of the QKHI. We introduce the Weber number We , a dimensionless quantity given by the ratio of the inertial force to the surface tension and extended to the segregated superfluids, to characterize the dynamics of the QKHI. This number is related to the ratio of the two above-mentioned length scales, separating the dynamical behavior between the universal macroscopic regime and the microscopic one. For

relatively small Weber number less than unity, the interface wave evolves to elongated flutter-finger patterns, as seen in the classical fluid dynamics. The fingers are disintegrated through the creation of quantized vortices at each tip of the fingers, supported by the fact that the vorticity along the interface with respect to one wavelength of the unstable wave is larger than a single quantum circulation $\kappa = h/m$. When the Weber number is typically larger than unity, the microscopic aspect of the interface structure becomes important in the nonlinear dynamics. We clarify the detailed characteristics of the pattern-forming dynamics from not only the simulations of the GP equations but also the linear stability analysis based on the Bogoliubov-de Gennes (BdG) equations. For the strongly segregated regime, a small-amplitude interface wave forms a zipper pattern and does not emit the quantized vortices at the tip of the wave, since the vorticity per wavelength is not enough to evolve a single vortex. However, the nonlinear dynamics causes multistep collapses of the interface, leading eventually to the turbulent state. When the intercomponent coupling strength is decreased to the miscibility limit, the interface instability exhibits a crossover from the KHI dynamics to the CSI-like behavior, as discussed in Ref. [8]. The analysis reveals the mechanism of frictional relaxation of the shear flow by forming a “sealskin” pattern through sheared CSI at the inhomogeneous overlapping region.

This paper is organized as follows. In Sec. II, we introduce the formulation and the setup of the problem to study the QKHI in phase-separated two-component BECs. Several characteristic length scales are introduced in order to classify different regimes of the nonlinear dynamics. In Sec. III, we introduce the Weber number and construct the phase diagram (Fig. 2) of the nonlinear dynamics. After that, we show the simulation results of the nonlinear dynamics associated with the shear-flow instability in Secs. IV and V for the small and large Weber numbers, respectively. Section VI is devoted to the conclusion and discussion.

II. FORMULATION

We first give a brief introduction of the QKHI in phase-separated two-component BECs. The details are found in Refs. [1,7,8]. Also we introduce the several length scales of the problem; in particular, the wavelength of the unstable interface mode and the interface thickness play an important role to understand the nonlinear dynamics.

A. Equations of motion

We consider two-component BECs in a homogeneous space without an external potential. In the mean-field theory at low temperatures, the two-component BECs are described by the condensate wave functions $\Psi_j(\mathbf{r}, t) = \sqrt{n_j(\mathbf{r}, t)}e^{i\theta_j(\mathbf{r}, t)}$ with the particle densities n_j and phases θ_j , obeying the coupled GP equations [38]

$$i\hbar \frac{\partial \Psi_j}{\partial t} = \left(-\frac{\hbar^2 \nabla^2}{2m_j} - \mu_j + g_j |\Psi_j|^2 + g_{j\bar{j}} |\Psi_{\bar{j}}|^2 \right) \Psi_j$$

$$(j, \bar{j} = 1, 2, \quad j \neq \bar{j}). \quad (1)$$

Here, m_j is the atomic mass and g_1 , g_2 , and g_{12} are the coupling constants in the nonlinear terms which are related to the s -wave scattering lengths a_1 , a_2 , and a_{12} , respectively, as $g_j = 4\pi \hbar^2 a_j / m_j$ and $g_{12} = 2\pi \hbar^2 a_{12} (m_1 + m_2) / m_1 m_2$. Throughout this work, we consider immiscible BECs under the condition $g_{12} > \sqrt{g_1 g_2}$ [39,40]. The immiscible ground state for the binary condensates with an equal particle number consists of the configuration in which one component occupies half of the space and the other does the rest; the stable interface is formed between them. We assume that the first and second components are located in $y \lesssim 0$ and $y \gtrsim 0$, respectively, and the interface between them is located near the $y \simeq 0$ plane.

The QKHI can be studied by making the linear stability analysis around the stationary state which has the straight interface at $y = 0$ and the shear flow velocities $\mathbf{v}_j = V_j \hat{x}$ with $V_1 = V_R/2$ and $V_2 = -V_R/2$, the relative velocity being determined as $V_R = |\mathbf{v}_1 - \mathbf{v}_2|$ along the x axis. Substituting the form $\Psi_j(\mathbf{r}) = \phi_j(y)e^{im_j V_j x / \hbar}$, the profile $\phi_j(y)$ can be calculated by solving the time-independent GP equations

$$\left(-\frac{\hbar^2}{2m_j} \frac{\partial^2}{\partial y^2} - \mu_j + \frac{m_j V_j^2}{2} + g_j |\phi_j|^2 + g_{j\bar{j}} |\phi_{\bar{j}}|^2 \right) \phi_j = 0. \quad (2)$$

Far from the interface, the bulk density for the j th component is simply given by the constant $n_{0j} = [\mu_j - m_j V_j^2 / 2] / g_j$, which is used as a boundary condition for the solution of Eq. (2).

B. The Kelvin-Helmholtz theory

There is one-to-one correspondence between classical hydrodynamics and the present system when one introduces the scalar velocity potential $\Phi_j = (\hbar/m_j)\theta_j$, the velocity field being given by $\mathbf{v}_j = \nabla \Phi_j$. From the GP equation (1), the equation of motion of Φ_j is written as

$$\frac{\partial \Phi_j}{\partial t} + \frac{v_j^2}{2} - \frac{\mu_j}{m_j} + P_j + Q_j = 0, \quad (3)$$

where $P_j = g_j n_j / m_j$ and $Q_j = -\hbar^2 (\nabla^2 \sqrt{n_j}) / (2m_j^2 \sqrt{n_j})$ represent the pressure function and the quantum pressure, respectively. When the quantum pressure term is neglected, we have a problem similar to the classical hydrodynamics of the KHI. The detail of the analysis has been described in Refs. [7,8]. Note that, in the standard problem in classical hydrodynamics, the interface between two species of fluids is stabilized by the gravitational potential, which is absent in our system.

We suppose that a position of the time-dependent curved interface can be described by the displacement field $y = \eta(x, z, t)$ and neglect the z dependence by assuming the uniformity along the z axis. A small-amplitude interface wave is represented by the localized small fluctuation of the velocity potential $\delta \Phi_j = \Phi_j - V_j x$ and the small displacement η with the form

$$\delta \Phi_j = A_j e^{(-1)^j k z} \cos(kx - \omega t), \quad (4)$$

$$\eta = B \sin(kx - \omega t), \quad (5)$$

where k and ω represent the wave number and the frequency of the interface wave, respectively. The dispersion relation of the interface wave is written as [7,8,41]

$$\omega = \frac{(\rho_1 V_1 + \rho_2 V_2)k}{\rho_1 + \rho_2} \pm \frac{1}{\sqrt{\rho_1 + \rho_2}} \sqrt{\alpha k^3 - \frac{\rho_1 \rho_2}{\rho_1 + \rho_2} V_R^2 k^2}. \quad (6)$$

Here, $k > 0$ and $\rho_j = m_j n_{0j}$ is the bulk mass density. The parameter α stands for the surface tension of the interface, corresponding to the excess energy due to the presence of the interface [42] and being determined later as a function of g_{12} .

When the inside of the square root in Eq. (6) becomes negative, the imaginary part $\text{Im}(\omega)$ appears and the shear flow states are dynamically unstable. From Eq. (6), the instability occurs for the nonzero relative velocity $V_R > 0$. The imaginary part $\text{Im}(\omega)$ appears in a range $0 < k < k_+$ with

$$k_+ = \frac{\rho_1 \rho_2}{\alpha(\rho_1 + \rho_2)} V_R^2. \quad (7)$$

The wave number of the most unstable (fastest growing) mode of the QKHI corresponds to

$$k_0 = \frac{2}{3} k_+ = \frac{2\rho_1 \rho_2}{3\alpha(\rho_1 + \rho_2)} V_R^2, \quad (8)$$

which means that $\text{Im}(\omega)$ takes a maximum at $k = k_0$.

In the following, we confine ourselves to the situation without the center-of-mass velocity of the two components, corresponding to the vanishing first term of the right-hand side of Eq. (6). The plus-minus sign represents the conjugate modes propagating to the opposite directions; we shall take only the plus sign below. If the center-of-mass velocity is alive, there is another critical velocity associated with the Landau instability given by the condition $\omega < 0$. Although this instability is significant when the system is subject to an energy dissipation as in the system of the superfluid helium [4–6], we will not consider this instability in the following by supposing the cold atom system which is almost isolated from a surrounded environment.

C. Characteristic length scales

Before the numerical simulations of the real time dynamics, it is instructive to understand the aspect of the dynamical instability and expected nonlinear dynamics by comparing the several characteristic length scales in our problem. In the following, we confine ourselves to the parameters as $m_1 = m_2 = m$ and $g_1 = g_2 = g$. We also assume the condition of the chemical potential as $\mu_1 - mV_1^2/2 = \mu_2 - mV_2^2/2 \equiv \mu$. Then, the number density in the bulk region is $n_1 = n_2 = \mu/g \equiv n_0$ and the mass density is written as $\rho_j = mn_0 = m\mu/g \equiv \rho$.

The first characteristic length scale is the healing length

$$\xi = \frac{\hbar}{\sqrt{2m\mu}}, \quad (9)$$

which determines the scale with which the amplitude of the wave function of the one component heals from zero to the bulk when the other component is absent. The healing length comes from a purely quantum origin, which is a balance between quantum pressure term and the nonlinear coupling

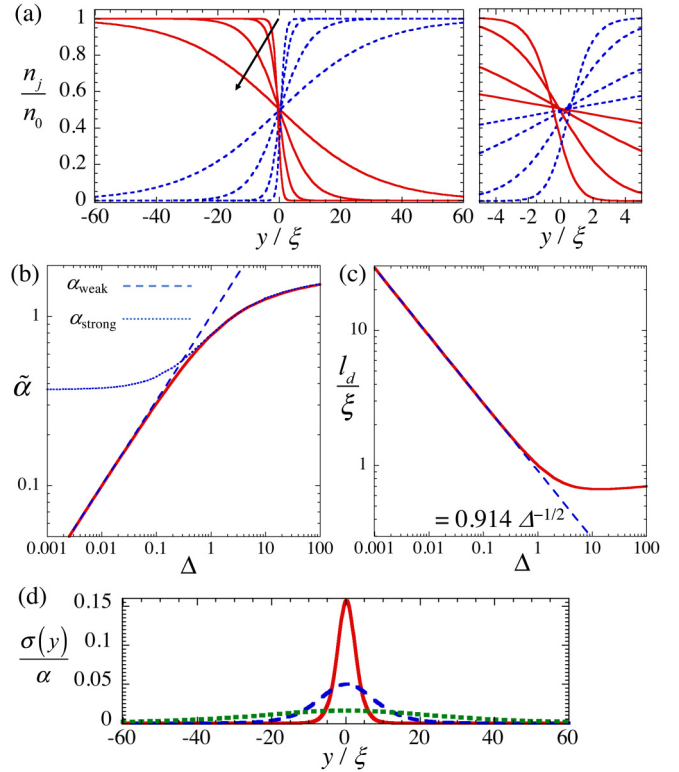


FIG. 1. The density profiles of the stationary solution of Eq. (2) are shown in the left panel of panel (a) for $\Delta = 1, 10^{-1}, 10^{-2}$, and 10^{-3} from the start to the end of the arrow. Here, the red solid and blue dashed curves correspond to $n_1 = |\phi_1|^2$ and $n_2 = |\phi_2|^2$, respectively, and their profiles are symmetric with respect to $y = 0$. The right panel shows the enlarged view of the left one around $y = 0$. Panels (b) and (c) show the surface tension $\tilde{\alpha} = \alpha/(2P_0\xi)$ and the thickness of the interface l_d/ξ as a function of $\Delta = (g_{12}/g) - 1$, respectively, by the (red) solid curves. In panel (b), we also plot the analytic formula of α_{weak} [Eq. (12)] and α_{strong} [Eq. (13)] by the thin dashed line and the thin dotted curve, respectively. In panel (c), we draw the fitting line $l_d/\xi = 0.914\Delta^{-1/2}$. The panel (d) shows the distribution of the surface tension density divided by α for $\Delta = 10^{-1}$ (red solid curve), 10^{-2} (blue dashed curve), and 10^{-3} (green dotted curve).

constant, providing a length scale not found in classical hydrodynamics. In this work, all lengths are scaled by ξ . By scaling the coordinate and the wave function as $\mathbf{r} \rightarrow \xi\mathbf{r}$ and $\phi_j \rightarrow \sqrt{n_0}\phi_j$, the stationary GP equation (2) has a single parameter g_{12}/g . Figure 1(a) shows the density profile of the stationary state for several values of the parameter $\Delta \equiv (g_{12}/g) - 1$. Although the interface is located at $y = 0$, there is a thickness of the interface since the density of the one component penetrates into that of the other component. The thickness of the interface is $\approx \xi$ for $\Delta \gg 1$, while it extends over from dozen to hundreds of times of ξ as $\Delta \rightarrow 0$. This thickness is determined more precisely in the following.

The second length scale is the wavelength of the growing interface displacement. We take this value as the inverse of the wave number of the most unstable mode:

$$\lambda_0 = \frac{2\pi}{k_0} = \frac{6\pi\alpha}{\rho V_R^2}, \quad (10)$$

k_0 being given by Eq. (8) with $\rho = \rho_1 = \rho_2$. The form of the surface tension α can be calculated by the excess ground potential per unit area due to the presence of the interface as [42,43]

$$\alpha = \int_{-\infty}^{+\infty} dy \sum_{j=1,2} \frac{\hbar^2}{m} \left| \frac{d\phi_j(y)}{dy} \right|^2 \equiv \int_{-\infty}^{+\infty} dy \sigma(y). \quad (11)$$

In Fig. 1(b), we show the value of α as a function of $\Delta \equiv g_{12}/g - 1 > 0$, where the numerical solution of $\phi_j(y)$ obtained from Eq. (2) is used to calculate Eq. (11). The approximate analytic formula of α without an external potential has been obtained as

$$\alpha_{\text{weak}} \simeq 2P_0\xi \sqrt{\frac{g_{12}}{g} - 1} \quad (12)$$

in the weakly segregating limit $g_{12}/g \simeq 1$ [44] and

$$\alpha_{\text{strong}} \simeq 4P_0\xi \left[\frac{2\sqrt{2}}{3} - 0.514 \left(\frac{g_{12}}{g} \right)^{-1/4} - 0.110 \left(\frac{g_{12}}{g} \right)^{-3/4} - 0.134 \left(\frac{g_{12}}{g} \right)^{-5/4} \right] \quad (13)$$

in the strongly segregating limit $g_{12}/g \gg 1$ [42,43]. Here, $P_0 = \mu^2/2g$ represents the equilibrium pressure. We confirm that the two analytical formulas can describe well the numerical result for the corresponding limits.

The surface tension density $\sigma(y)$ in Eq. (11) is localized around the position of the interface, as shown in Fig. 1(d). From the distribution of $\sigma(y)$, we can obtain the third length scale

$$l_d = \sqrt{\frac{\int dy [y^2 \sigma(y)]}{\alpha}}, \quad (14)$$

which represents the thickness of the interface. Figure 1(c) shows l_d as a function of Δ . In the weakly segregating limit ($\Delta \ll 1$), we have $l_d \sim \xi/\sqrt{\Delta}$, consistent with the analytical evaluations in Refs. [40,42,44], where the total density $n_1 + n_2$ is almost uniform. With increasing Δ in the strongly segregating regime ($\Delta \gg 1$), l_d takes a minimum $l_d \approx 0.67\xi$ around $\Delta \simeq 10$ and approaches slowly the value $\approx 0.8\xi$, which is obtained in the limit $\Delta \rightarrow \infty$. The latter behavior is due to the fact that, after the interface becomes thinnest, the condensate domains are repelled further to get rid of the overlapping region completely, which leads to the imperceptible increase of l_d . At $\Delta \rightarrow \infty$ the total density at the interface becomes zero and the profile is given by the dark-soliton solution [42].

III. PHASE DIAGRAM BASED ON WEBER NUMBER

A. Weber number

In the classical hydrodynamics, when discussing the interface dynamics of the phase separated fluid, the Weber number

$$\text{We} = \frac{\rho V_R^2 L}{\alpha}, \quad (15)$$

which is the ratio of the inertial force of the fluid to the surface tension force, is a useful dimensionless quantity to

characterize the nonlinear dynamics [45,46]. The Weber number includes the characteristic length L , which is taken as the wavelength of the initial perturbation in the classical case.

In our simulations below, since the dynamical instability is caused by the random noise, L is naturally given by λ_0 . Then, the Weber number is simply given by $\text{We} = 6\pi$ (=const.) from Eq. (10), which is not suitable to classify the dynamics of our problem. Instead of using λ_0 , we take here the interface thickness as the length scale $L = l_d$; the Weber number in our problem is thus written as

$$\text{We} = \frac{6\pi l_d}{\lambda_0}. \quad (16)$$

This definition is generally applicable to any system in terms of the thickness of the interface between two separated fluids.

The thickness l_d depends on the system parameters through the internal structure of the interface described by the ‘‘microscopic theory’’ beyond the hydrodynamic theory of KHI. In our case, the structure and thus the thickness are uniquely determined by the dimensionless parameter Δ . In this sense, the definition of the Weber number as Eq. (16) enables us to access more microscopic behavior of the instability beyond the KH theory. In fact, according to the conditions under which the KH theory holds, the hydrodynamic treatment breaks down when λ_0 is similar or less than l_d ; namely, $\text{We} > 1$. We demonstrate that the microscopic behavior described by quantum fluid dynamics becomes prominent typically for $\text{We} > 1$.

B. Phase diagram

Here, we summarize the prospect of the nonlinear dynamics in terms of Weber number by comparing the simulation results in past works [7,8,29]. We show the phase diagram of the dynamics in the Δ - V_R^2 plane in Fig. 2. Here, V_R is scaled by the characteristic velocity $V \equiv \xi\mu/\hbar = \sqrt{\mu/(2m)}$. Some contours of the typical values of We are also shown. Since Eq. (16) means $V_R^2 \propto \alpha/l_d$ for a given We , the contour lines of We have a behavior $V_R^2 \propto \Delta$ in the weakly segregating limit with $\alpha_{\text{weak}} \propto \Delta^{1/2}$ and $l_d \propto \Delta^{-1/2}$.

The (red) solid curve $k_0 l_d = 1$ [$\text{We} = 4$ from Eq. (16)] gives roughly the boundary of two characteristic nonlinear dynamics. For $k_0 l_d \lesssim 1$ or $\text{We} \lesssim 1$ (the lower-right region of the diagram) the interface is thin and the linear stability is well described by the KH theory. On the other region with $k_0 l_d \gtrsim 1$ or $\text{We} \gtrsim 1$, the thickness of the interface is larger than the wavelength of the excitation so that the resulting instability cannot be described by the KH theory in which the internal structure of the interface is neglected. We also depict two other (blue dashed and green dotted) curves that classify the different dynamical regimes associated with the characteristic pattern formation, which are derived in the following sections. Note that these curves provide rough boundaries, not rigid ones, between the displayed patten formation, since the dynamical behavior exhibits a crossover-like transition with respect to the parameter change.

There are some studies showing the simulation results of the nonlinear dynamics of the KHI. Takeuchi *et al.* [7]

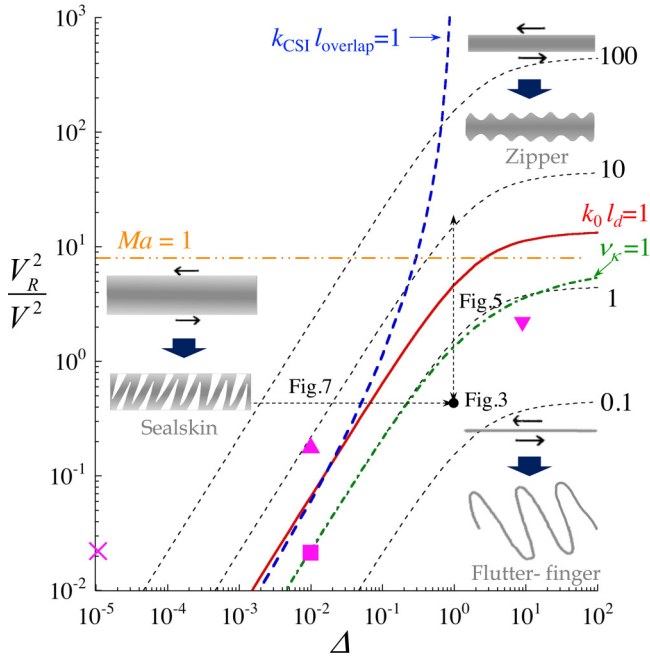


FIG. 2. The expected phase diagram of the dynamical pattern formation by the shear flow instability in the Δ - V_R^2 plane. The resulting pattern is schematically depicted in each region, where the gray region represents the interface between the binary superfluids. We also show the contours of the typical Weber number We by the dashed curves. The red solid curve represents the relation $k_0 l_d = 1$, which divide roughly the two characteristic regions of the instability. For $k_0 l_d \lesssim 1$ ($We \lesssim 1$) corresponding to the right side of the red curve, the instability of the thin interface is well described by the classical KHI. In the left side with $k_0 l_d \gtrsim 1$ ($We \gtrsim 1$), the interface becomes thick so that the KH theory is not directly applicable. The green dashed-dotted curve shows the relation $v_\kappa \equiv \lambda_0 V_R / 2\kappa = 1$; see the discussion in Sec. IV C. The orange dashed double-dotted line represents $Ma = 1$ with the Mach number Ma of the bulk flow, which is supersonic above this line. The blue dashed curve shows the relation $k_{CSI} l_{overlap} = 1$; see the discussion in Sec. VI. The parameter points given in the previous papers are shown by the symbols: \blacktriangledown Fig. 1 in Ref. [7], \blacktriangle Fig. 8 in Ref. [29], \blacksquare Fig. 2(a) in Ref. [8], and \times Fig. 2(b) in Ref. [8]. The black dot and the dashed arrows represent the parameter range along which we show the numerical results in the following sections.

considered the KHI in a strongly segregated condensates with $\Delta = 9$ and $V_R = 0.98 \times \sqrt{2}V$, where the authors also introduced an external potential to sustain the stable interface. The simulation results demonstrated that the initially growing sinusoidal wave deformed into a sawtooth wave. The vorticity increased on the edges of the sawtooth waves, developing as a quantized vortex and being released into each bulk. The subsequent paper by Suzuki *et al.* [8] showed that the dynamics for $V_R = \sqrt{2} \times 10^{-1}V$ and two different values of Δ , namely $\Delta = 10^{-2}$ and $\Delta = 10^{-5}$, which aimed to discuss the dependence of the interface thickness of the nonlinear dynamics. There, the dynamics exhibits a crossover-like behavior between the KHI and the CSI; in the latter, the instability of the density wave arises in the overlapping region of the two components. Finally, Kovyakov *et al.* [29] showed the

dynamics for $\Delta = 10^{-2}$ and $V_R = V/3$.¹ They observed that, after the periodic interface wave is excited, the vorticity accumulated on the mode with the largest wavelength in the system to make a vortex bundle in the latter stage, which is similar to the role-up pattern seen in the classical KHI. We have also observed similar role-up patterns in the latter stage of the instability for different parameter regimes in our simulations. This behavior is conventionally explained by the fact that a bundle of quantized vortices can be regarded as a coarse-graining vortex in classical fluids. This scenario would be universal in the latter stage of quantum KHI when the system can form a large vortex bundle without external potentials and we thus focus on the nonlinear dynamics in the early stage before forming the roll-up patterns.

IV. UNIVERSAL MACROSCOPIC REGIME ($We \lesssim 1$)

In this section and the next one, we demonstrate the nonlinear dynamics by numerically solving the time-dependent GP equation (1) to corroborate the phase diagram of Fig. 2. We study the dynamics in the 2D system by assuming the uniformity along the z axis and do not consider a contribution of an external trap. Here, we show the dynamics of the interface for $We \lesssim 1$, namely, the lower-right region of Fig. 2 (the large Δ and the small V_R). In this regime, referred to as the universal macroscopic regime hereafter, the interface thickness l_d is smaller than the wavelength λ_0 of the KH theory; the nonlinear dynamics has a similarity with the KHI-induced dynamics in classical hydrodynamics,

The numerical calculations are done under the following procedures. We first solve Eq. (2) through the imaginary time propagation to obtain the stationary solution $\phi_j(y)$. Setting the initial wave function as $\Psi_j(x, y, t = 0) = \phi_j(y)e^{imV_j x/\hbar}$ with $V_j = (-1)^{j-1}V_R/2$, we then solve Eq. (1) to see the time developments of $\Psi_j(x, y, t)$ for given values of V_R and Δ , where the simulations are done in a 2D x - y system with the size $[-L_{x,y}, +L_{x,y}]$. The periodic boundary condition is given for the x direction along which the condensates initially have uniform counterflow, while the Neumann boundary condition is given at $y = \pm L_y$. The system size (L_x, L_y) is prepared properly for each parameter set enough to omit the influence of numerical boundaries. To initiate the dynamical instability, we give a small random noise (of the order 10^{-5}) to the initial wave functions. The movies of the dynamics can be seen in the Supplemental Material [47].

A. Flutter-finger pattern

The dynamics can be visualized directly through the profile of the condensate density. We show the density difference $\Delta n = (n_1 - n_2)/n_0$ below, in which the bulk region of the first (second) component corresponds to $\Delta n \simeq 1$ (-1),

¹In Ref. [29] the initial wave functions for the component $j = 1, 2$ have phase factors $e^{-i(-1)^j q_0 x}$ with the wave number q_0 . Thus, the relative velocity is given by $V_R = 2\hbar q_0/m$. The value of q_0 is taken as $q_0 = 2.5a_z^{-1}$ with the harmonic-oscillator length $a_z = \sqrt{\hbar/(m\omega_z)}$. Then, $V_R/V = 2\sqrt{2}q_0 a_z \sqrt{\hbar\omega_z/\mu} = 4q_0 a_z/R_0$ with the Thomas-Fermi radius R_0 . When $q_0 a_z = 2.5$ and $R_0 = 30$ in Ref. [29], we have $V_R/V = 1/3$.

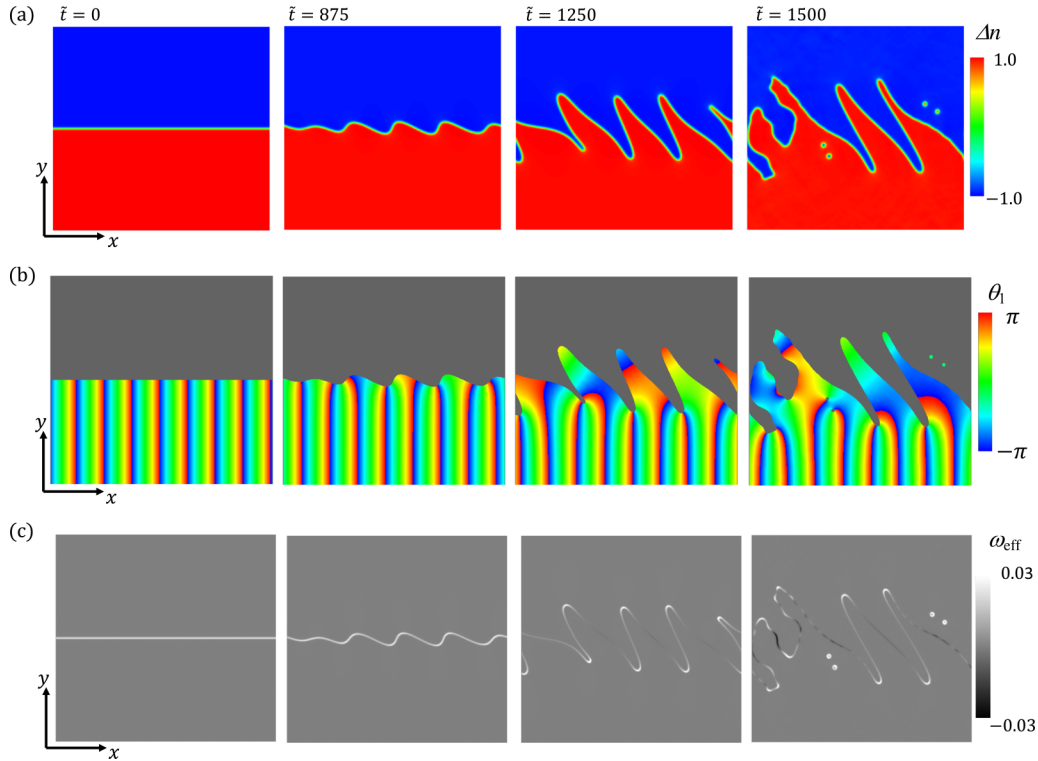


FIG. 3. Snapshots of the unstable dynamics for $V_R/V = \sqrt{0.45}$ and $\Delta = 1.0$, where the corresponding Weber number is $We = 0.291$. In panel (a), the density difference $\Delta n = (n_1 - n_2)/n_0$ is depicted, in which the red (blue) region corresponds to the area where the density n_1 (n_2) is located. In panel (b), the profile of the phase θ_1 of the first component is shown only in the region $\Delta n > 0$; there is only noisy phase fluctuations in the region $\Delta n < 0$ since the amplitude n_1 is almost zero there. A vortex is located at the endpoint of a branch cut (jump from $\theta_1 = -\pi$ to π). The distributions of the vorticity ω in the x - y plane is shown in panel (c). The spatial region of the plot is $-150\xi \leq x, y \leq 150\xi$. The time is represented by the dimensionless value $gn_0t/\hbar \equiv \tilde{t}$.

while the interface is distributed around $\Delta n = 0$. Figure 3(a) shows a typical dynamics of the condensate density for $\Delta = 1.0$ and $V_R/V = \sqrt{0.45} \approx 0.67$. In this parameter, the instability begins to grow after $\tilde{t} \equiv (gn_0/\hbar)t \simeq 800$, where the amplitude of the sinusoidal interface wave is monotonically increased due to the exponential growth with $\text{Im}(\omega) \neq 0$ described by Eq. (6). The wavelength given by the analytical prediction of Eq. (10) is $\lambda_0 \approx 64.9\xi$, reasonable agreement with the numerical result $\approx 60\xi$ in the panel at $\tilde{t} = 875$ Fig. 3(a). Then, the sinusoidal wave develops finger patterns. Although the formation of such a finger pattern has been seen in the simulations of the classical fluid dynamics [45,46], the subsequent nonlinear evolution exhibits a quite different behavior from that of the classical one. The fingers are elongated gradually in the oblique direction and eventually disintegrate into bubble-like domains of the condensates.

For $We \lesssim 1$, the eigenmode of the unstable excitation is localized on the interface; the associated density modulation occurs periodically along the interface [8]. This means that the form of the excitation is sinusoidal in the early stage of the instability. After the amplitude of the interface wave becomes large to form a finger pattern, the finger regions are pushed by the other counterflowing components, like a grass fluttered in the wind. Thus, the fingers of the component 1 (2) grow along the upper left (lower right) direction in the nonlinear stage of the evolution. We call this stripe pattern as the “flutter-finger” pattern.

Figure 3(b) shows the corresponding phase profile $\theta_1 = \arg(\Psi_1)$ of the first component. Each bubble-like domain contains a quantized vortex, as seen in the panel at $\tilde{t} = 1500$ of Fig. 3(b), forming a coreless vortex [48,49] with the vortex core filled by the density of the other component. Also, one can see that the branch cuts are located near the tips of the fingers of the Ψ_2 domain as precursors of the vortices. The emission of the quantized vortices from the finger pattern is a distinguishable feature from the classical problem.

B. Surface vorticity

The appearance of the finger patterns involves the characteristic vorticity distribution, which eventually develops to the quantized vortices. To show this, we introduce the mass current velocity defined as

$$\mathbf{v} = \frac{\rho_1 \mathbf{v}_1 + \rho_2 \mathbf{v}_2}{\rho_1 + \rho_2} \quad (17)$$

and the associated vorticity

$$\boldsymbol{\omega} = \nabla \times \mathbf{v}, \quad (18)$$

which provide a useful description of vortices in the two-component system [7,50]. In the 2D calculation, we are concerned only with the z component as $\boldsymbol{\omega} = \omega(x, y)\mathbf{e}_z$.

Figure 3(c) shows the distribution of the vorticity $\omega(x, y)$. Initially, the vorticity is distributed uniformly along the

interface, which forms a linear vortex sheet. The circulation per a unit length along the sheet, denoted as ρ_Γ , can be easily calculated according to the Stokes theorem as

$$\rho_\Gamma = \int d\mathbf{S} \cdot \boldsymbol{\omega} = \int d\boldsymbol{\ell} \cdot \mathbf{v} = v_1 - v_2 = V_R. \quad (19)$$

Here, the area of the integral is taken as a rectangular enclosing the vortex sheet and having a unit horizontal width and a vertical width sufficiently larger than the interface thickness. As shown in Appendix A, these vorticity distribution can be understood according to the analogy to the electrostatic problem. Far from the interface, \mathbf{v} is coincident with \mathbf{v}_j appearing in Eq. (3), and if the time and spatial scale is slow, \mathbf{v} satisfies the Laplace equation. Then, the vorticity distribution ρ_Γ on the sheet has a one-to-one correspondence with that of an electronic charge on a flat-plate conductor, being obtained by solving the Laplace equations with the suitable boundary condition.

This electrostatics analogy is approximately applicable to our dynamic situation, in which the vorticity is accumulated at the tip of each finger to form quantized vortices (see the panel at $\tilde{t} = 1250$) during the slow growth of the finger pattern. The electrostatics predicts that a surface charge density becomes larger on a sharp end of a charged object than that on the other region [51]; see also the discussion in Appendix A. The accumulation of the vorticity is thus enhanced as the fingers grow and, when the local accumulated vorticity becomes comparable to the single quantum circulation $\kappa = h/m$, the vortices are eventually emitted from the tip and the fingers undergo self-collapse. After the vortices are emitted, the vorticity on the sheet is reduced even to negative values locally according to the conservation of the vorticity.

The vorticity charged per a single interface wave is also an important quantities to understand the pattern formation. To make a vortex from a single finger, the vorticity per a half of the unstable wavelength should contain the vorticity above the quantum circulation $\kappa = h/m$. Since an interface per a unit wavelength possesses a vorticity $\rho_\Gamma \lambda_0$ and two fingers can grow from a single wave, the quantity $\lambda_0 \rho_\Gamma / (2\kappa) \equiv \nu_\kappa$ determines whether an elongated finger possesses vorticity enough to make a quantized vortex. Using the relation of Eq. (19), we also plot the curve $\nu_\kappa = 1$ in the diagram of Fig. 2, whose behavior is almost coincident with the curve $We \simeq 1$. This is because the relation $\nu_\kappa = 1$ can be written as $(V_R/V)^2 = 9\tilde{\alpha}^2/4$, which has a similar dependence of We with respect to Δ in the weakly segregating limit $\alpha_{\text{weak}} \propto \Delta^{1/2}$. For $We < 1$, in the right side of this curve, the vortex sheet in one finger contains the vorticity enough to generate a single quantized vortex. Then, the event of the vortex generation takes place in the first growing process of the fingers. In the other regime with $We > 1$, the initially growing hump of an interface wave does not contain the vorticity enough to make a vortex and the vortices cannot be emitted from the first growth of the wave. These are clear distinctive features of the late-stage dynamics in the QKHI compared with the classical KHI. As seen in the next section, the multistep destabilization is necessary to emit vortices from the interface region for $We > 1$.

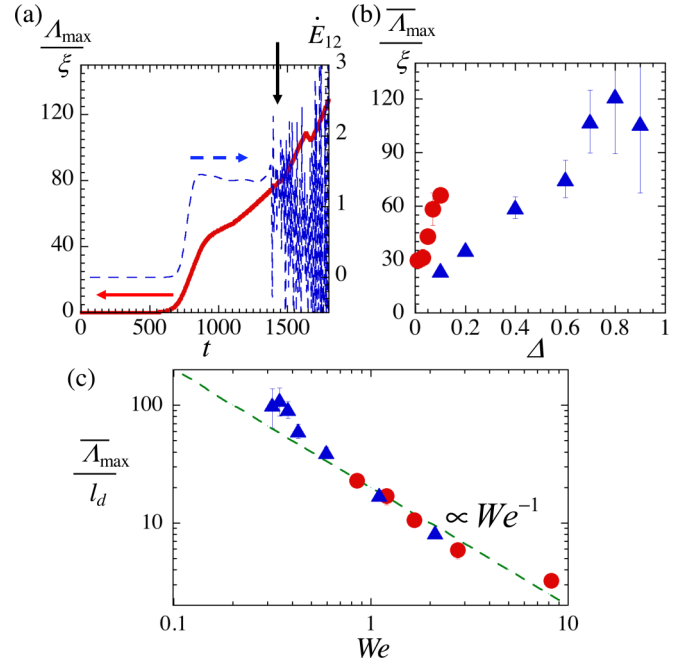


FIG. 4. Maximum length Λ_{max} of the growing fingers before the vortex emission. Panel (a) shows a single shot data of the time development of the finger length Δ as well as that of the time derivative of the intercomponent interaction energy $\dot{E}_{12} = dE_{12}/dt$ for $V_R/V = \sqrt{0.45}$ and $\Delta = 0.6$. The length Λ_{max} is extracted at the moment when \dot{E}_{12} starts to make a rapid chaotic oscillation, denoted by the downward arrow. Panel (b) shows $\bar{\Lambda}_{\text{max}}$, an average with five different initial conditions for a single plot, as a function of Δ for $V_R/V = \sqrt{0.18}$ (red circles) and $\sqrt{0.45}$ (blue triangles), where the error bars represent the standard deviation. The bottom panel (c) shows $\bar{\Lambda}_{\text{max}}$ as a function of the Weber number We , where $\bar{\Lambda}_{\text{max}}$ is scaled by l_d . The green dashed line serves as a guide to the eye for the We^{-1} dependence.

C. Universal scaling

To capture a character of the wave pattern formation, we focus on the length of the fingers seen in the simulations. Here, the finger length Λ is defined as the difference between the amplitude at the highest top and that at the lowest bottom of the interface wave, where the interface position is identified by zeros of the density difference Δn . We extract the maximum length Λ_{max} at the moment when the first self-collapse of the fingers takes place. The timing of the first self-collapse is related to the time evolution of the total length of the interface because the evolution changes qualitatively after the vortex nucleation. The interface length is roughly proportional to the intercomponent interaction energy $E_{12} = (1 + \Delta) \int d\mathbf{r} |\Psi_1|^2 |\Psi_2|^2$, since the two components overlap only in the interface layer. The time derivative $\dot{E}_{12} = dE_{12}/dt$, shown in Fig. 4(a) as a typical example, indicates the first exponential growth of the interface wave at $\tilde{t} \approx 700$ and the subsequent nonlinear elongation of the fingers for $700 \lesssim \tilde{t} \lesssim 1400$. The growth of the fingers is suppressed by the creation of the quantized vortices; a signal of the vortex creation can be seen as an occurrence of a rapid chaotic oscillation of \dot{E}_{12} and we take the value Λ_{max} at this moment.

Figure 4(b) shows the average $\bar{\Lambda}_{\max}$ taken from the five simulations with a random initial noise. We find that the length of the growing fingers can be elongated further with increasing Δ for a fixed V_R . For smaller V_R , the maximum length of the finger patterns increases rapidly with the increase in Δ , where the measured finger length exhibits large error bars. The growth time of the instability becomes extremely long in the limit of $\Delta \gg 1$ and $V_R \ll 1$, the numerical demonstration being difficult there. As shown in Fig. 4(c), the results are explained more clearly by plotting $\bar{\Lambda}_{\max}/l_d$ with respect to the Weber number, where the data are well described by the We^{-1} behavior. Thus, Fig. 4(c) explains not only the fact that the finger length decreases with We , but also the fact that the Weber number can give a common index to characterize the nonlinear dynamics of the KHI for different parameter values. For example, the qualitative behavior of the dynamics is common between our Fig. 3 and Fig. 2(a) in Ref. [8], which are done with the different system parameters but nearly equal We . The behavior $\bar{\Lambda}_{\max}/l_d \propto We^{-1}$ implies $\bar{\Lambda}_{\max} \propto \lambda_0$ from Eq. (16), which means that the maximum amplitude of the interface wave is as large as its wavelength.

V. MICROSCOPIC REGIME: $We \gtrsim 1$

Next, we consider the dynamics of the interface by increasing We much larger than unity. This regime, referred to as the microscopic regime, corresponds to the condition that the interface thickness l_d is larger than the wavelength λ_0 of the KH theory. We find that, even though We is common, the nonlinear dynamics in this regime are qualitatively different for strongly and weakly segregated cases in the microscopic regime; we discuss separately these situations in the following.

The KH theory is not applicable directly to this regime, since it is based on the assumption of the thin interface thickness compared with the other length scales. Thus, we analyze the BdG equation numerically to see the interface instability against a shear flow more microscopically. We linearize the time-dependent GP equation (1) around the stationary solutions ϕ_j^0 as

$$\Psi_j = [\phi_j^0(y) + u_j(y)e^{ikx-i\omega t} - v_j^*(y)e^{-ikx+i\omega^*t}]e^{imV_j x/\hbar} \quad (20)$$

to obtain the BdG equation

$$\hat{\mathcal{H}}\mathbf{u} = \hbar\omega\mathbf{u}, \quad (21)$$

$$\hat{\mathcal{H}} = \begin{pmatrix} \hat{h}_1^+ & -g(\phi_1^0)^2 & g_{12}\phi_1^0\phi_2^{0*} & -g_{12}\phi_1^0\phi_2^0 \\ g(\phi_1^{0*})^2 & -\hat{h}_1^- & g_{12}\phi_1^{0*}\phi_2^{0*} & -g_{12}\phi_1^{0*}\phi_2^0 \\ g_{12}\phi_1^{0*}\phi_2^0 & -g_{12}\phi_1^0\phi_2^0 & \hat{h}_2^+ & -g(\phi_2^0)^2 \\ g_{12}\phi_1^{0*}\phi_2^{0*} & -g_{12}\phi_1^0\phi_2^{0*} & g(\phi_2^{0*})^2 & -\hat{h}_2^- \end{pmatrix}, \quad (22)$$

where $\mathbf{u} = (u_1, v_1, u_2, v_2)^T$ and

$$\hat{h}_j^\pm = -\frac{\hbar^2}{2m} \left[\frac{\partial^2}{\partial y^2} - \left(k \pm \frac{mV_j}{\hbar} \right)^2 \right] - gn_0 - \frac{mV_j^2}{2} + 2g|\phi_j^0|^2 + g_{12}|\phi_j^0|^2 \quad (23)$$

[$\bar{j} = 1(2)$ for $j = 2(1)$]. We numerically diagonalize the discretized BdG Hamiltonian $\hat{\mathcal{H}}$ to calculate the eigenfrequency

ω for a given value of k , the wave number of the plane-wave excitation along the translationally invariant x axis. The interface mode is described by the eigenmodes $[u_j(y), v_j(y)]$ localized around the interface in the y direction. When the frequency has a nonzero imaginary part $\text{Im}[\omega] \neq 0$, the system is dynamically unstable.

In the previous study [8], the BdG spectrum was compared between the miscible condensates with external gradient potential and immiscible ones without potential in connection with CSI. For comparison we use the dispersion relation of the counterflowing miscible condensates in a homogenous system, referred to as homogeneous CSI; the dispersion is given by [32–34]

$$(\hbar\omega)^2 = \varepsilon_0(\varepsilon_0 + 2gn) + \varepsilon_R^2 \pm 2\sqrt{\varepsilon_0\varepsilon_R^2(\varepsilon_0 + 2gn) + (g_{12}n)^2\varepsilon_0}, \quad (24)$$

with $\varepsilon_0 = \hbar^2 K^2/(2m)$, $\varepsilon_R = \hbar k_{\parallel} V_R/2$, and $n = n_1 = n_2$ is the miscible condensate density. The wave number $\mathbf{K} = (k_{\parallel}, k_{\perp})$ consists of the components parallel and perpendicular to the relative velocity V_R . Here, we have denoted for clarity the wave number parallel to V_R as k_{\parallel} which corresponds to k appearing before. Beyond a certain value of V_R , $\hbar\omega$ becomes purely imaginary and the system is dynamically unstable. The more information of the CSI is described in Ref. [34] and is briefly summarized in Appendix B. We apply this formula to our partially overlapping condensates in the immiscible regime in the spirit of the local density approximation.

A. Zipper pattern formation

1. Development of the density and the phase

First, we show the simulation results of the GP equations in the strongly segregating regime. The typical numerical results are shown in Fig. 5, where we increase V_R with fixed $\Delta = 1$ from the parameters of Fig. 3. For $V_R/V = 2$ in Fig. 5(a), the initially growing interface wave forms a sawtooth shape. Then, the sawtooth pattern transforms to a transient zipper pattern, where each cusp is torn off from the hump and just slides to merge with the next hump, instead of emitting the vortices at the tip of the interface wave. After that, the dynamics exhibits a recurrence of the sawtooth and zipper patterns alternatively. However, the periodic pattern is disturbed in the long-time nonlinear evolution, eventually evolving a large-scale turbulent structure. A further increase in V_R results in the growth of the sawtooth pattern with a shorter wavelength, as shown in Fig. 5(b) depicting the dynamics for $V_R/V = \sqrt{20}$. The transient zipper pattern again results from the sliding motion of the humps, and also there appears a density filament in the bulk region [the panel at $\tilde{t} = 62.5$ in Fig. 5(b)]. After the zipper pattern and the filaments appear, the interface deforms furthermore with larger length scales [the panel for $\tilde{t} = 75$ in Fig. 5(b)] and evolves the turbulent structure.

The absence of the vortex emission during the first growth of the instability is due to the fact that v_k in these parameters is less than unity; a half of the wavelength of the interface does not contain enough vorticity to generate a single quantized vortex. Figure 5(c) shows the evolution of $\theta_1 = \arg(\psi_1)$ corresponding to Fig. 5(b). It is clear that the number of density humps is incommensurate with that of the branch cuts that

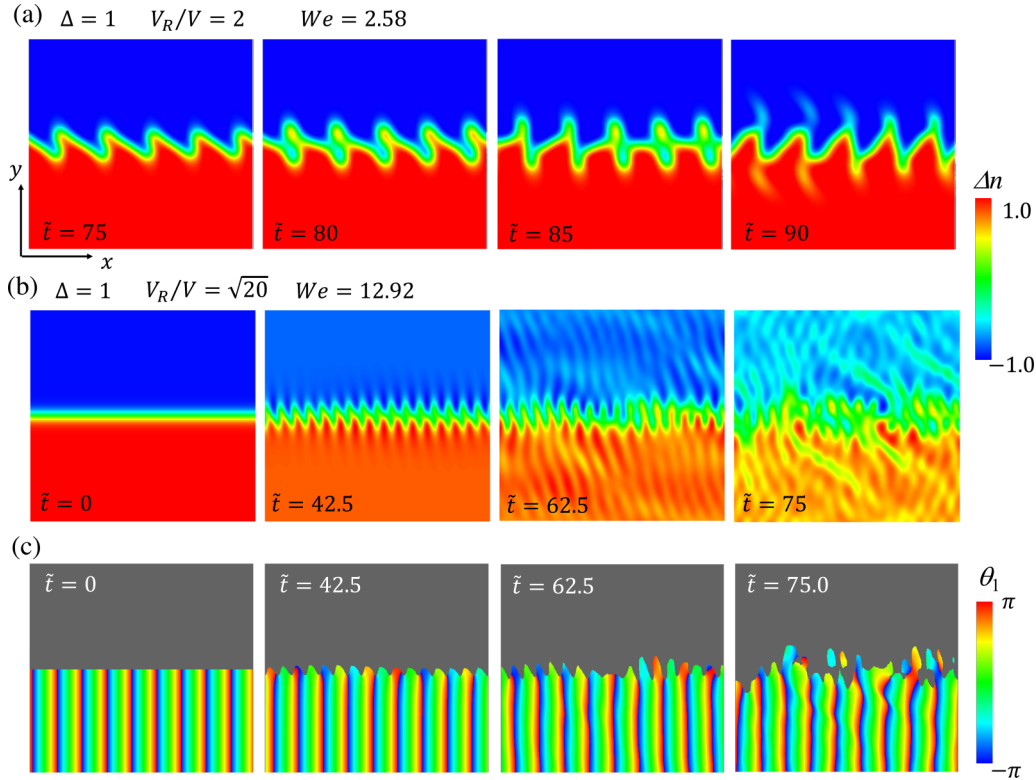


FIG. 5. Typical dynamics of the density difference Δn in the case of strongly phase-separated condensate with $\Delta = 1.0$ and the relative velocity (a) $V_R/V = 2$ ($We = 2.58$) and (b) $V_R/V = \sqrt{20}$ ($We = 12.92$). The red (blue) region corresponds to the area where the density n_1 (n_2) is located. The profile of the phase θ_1 in the region with $\Delta n > 0$, corresponding to panel (b), is shown in panel (c). The spatial region of the plot is $-25\xi \leq x, y \leq 25\xi$.

will evolve to quantized vortices; see Fig. 3(b) for comparison. This is consistent with $v_\kappa < 1$ and thus each density hump does not emit a vortex but forms the zipper pattern. In this sense, the occurrence of the zipper pattern is a characteristic phenomenon of strongly segregated condensates in the microscopic regime.

Note that, in the case of Fig. 5(b), the Mach number in the bulk region $Ma = V_j/\sqrt{\mu/m} = V_R/(2\sqrt{2}V)$ is more than unity. Thus, the bulk flow is supersonic so that the density filament can be identified as an appearance of a shock wave. Usually, a Mach cone structure is generated by an obstacle forced to move through a superfluid with supersonic velocity [52–55]. Since there is no forced obstacle in our case, it does not lead to the clear formation of a Mach cone.

2. The results of the Bogoliubov-de Gennes analysis

The spectrum of the BdG equation is useful to understand the numerical observation. We show in Fig. 6 the imaginary part $\text{Im}[\omega]$ of the eigenfrequency as a function of k for $\Delta = 1$ and several values of V_R . Since there is not an external potential, the imaginary part always appears for $V_R \neq 0$ in the range $0 < k < k_{\text{max}}$. For small values of $V_R \lesssim 1$, an example being shown in Fig. 6(a) for $V_R/V = 1$, there is a single branch associated with the dynamical instability, which is consistent with Eq. (6) of the KH theory.

However, the spectrum is deviated from Eq. (6) with increasing $V_R \gtrsim 1$. In Fig. 6(b), we see that $\text{Im}[\omega]$ of the BdG result for $V_R/V = 2$ lies deeply inside the dispersion

curve of Eq. (6). We confirm that the peak of $\text{Im}[\omega]$ of the BdG result determines the wavelength k_0^{BdG} of the growing wave; for example, we have $k_0^{\text{BdG}}\xi = 0.592$ ($\lambda_0^{\text{BdG}}/\xi = 10.6$) for $V_R/V = 2$, reasonably in agreement with the results of Fig. 5(a). It is thus suggested that the behavior of Fig. 5(a) deviates from the KH theory. Above a certain value of V_R , a main branch is shifted to the higher- k region and there appear many sub-branches to form a complicated spectral form, as shown in Fig. 6(c) for $V_R/V = \sqrt{20}$. The main peak appears at $k_0^{\text{BdG}}\xi = 1.939$ for $V_R/V = \sqrt{20}$; the corresponding wavelength $\lambda_0^{\text{BdG}}/\xi = 3.239$ is again reasonably in agreement with the spatial period ≈ 2.9 of the pattern at $\tilde{t} = 42.5$ seen in Fig. 5(b). Although the initial growth rate of the unstable dynamics is determined by the main peak in the BdG spectrum, the subsequent evolution is affected by the excitations of the unstable sub-branch distributed in a wider range of the wave number, which leads to the multistep growth of the instability and complicated nonlinear dynamics.

Note that the main unstable branch of $\text{Im}[\omega]$ resembles the imaginary part of the CSI dispersion Eq. (24). To this end, we use $g_{12} = 2g$ and $n = n_0(0.5 - \delta)$ at the center of the interface ($y = 0$), where δ takes a finite value $0 < \delta < 0.5$ ($\delta \approx 0$ for $\Delta \ll 1$ and $\delta = 0.5$ for $\Delta \rightarrow \infty$) extracted from the numerical solution [see the right panel of Fig. 1(a)]. This implies that the instability in the microscopic regime $We > 1$ can be described by the CSI even for the strongly segregating regime. In the theory of the CSI, for $2\sqrt{2}(1 - g_{12}/g) < V_R/V < 2\sqrt{2}(1 + g_{12}/g)$ the unstable region is broadly distributed in the wave-number space (k_\parallel, k_\perp) , while for

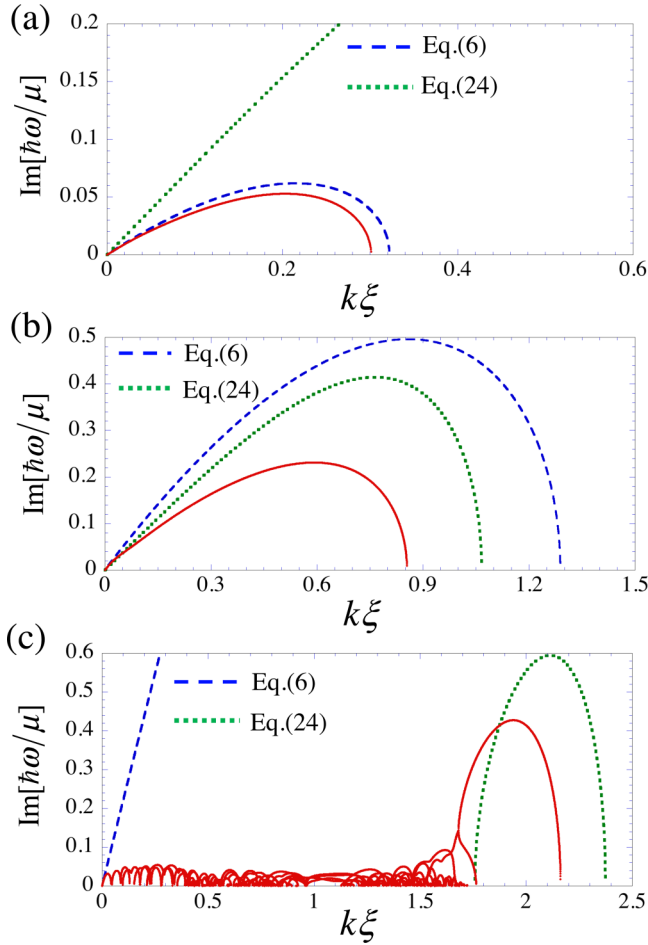


FIG. 6. The imaginary part of the excitation spectrum, $\text{Im}[\omega]$, of the BdG equations for $\Delta = 1.0$ and (a) $V_R/V = 1$, (b) 2, and (c) $\sqrt{20}$, shown by the red dots. The blue dashed curve represents Eq. (6) obtained by the KH theory in Sec. II B. The green dotted curve represents Eq. (24) in the theory of the CSI in Ref. [34], where $n = 0.318n_0$ [taken from Fig. 1(a)], $g_{12} = 2g$, and $k_{\perp} = 0$.

$V_R/V > 2\sqrt{2(1 + g_{12}/g)}$ the unstable region appears in the narrow region in the wave-number space $(k_{\parallel}, k_{\perp})$ as a crescent shape [34]; see Fig. 10 in Appendix B. Since the CSI can occur with the overlapping region between the two components, the appearance of eigenmodes with finite k_{\perp} is suppressed for $\Delta = 1$, where the excitations are well localized in a small overlapping region. Thus, the branch of the main peak in the higher- k range can be described mainly by Eq. (24) with $k_{\perp} = 0$; the minor contributions distributed in the lower- k range in Fig. 6(b) is considered as originating from the excitations with $k_{\perp} \gtrsim 2\pi/l_d$.

B. Sealskin pattern formation

With decreasing $\Delta \rightarrow 0$, the interface thickness l_d is increased. The previous paper has investigated the KHI -CSI crossover [8], where the authors found the continuous change of the V_R dependence of the unstable range of the wave number $0 < k < k_+$ from the KHI with $k_+ \propto V_R^2$ [see Eq. (7)] to the CSI with $k_+ \propto V_R$, which has been confirmed by the BdG analysis. However, we show here that the theory of CSI is not

simply applicable due to a difference in the mechanism of the frictional relaxation of the relative motion between our system and the CSI in uniform systems.

1. Development of the density and the phase

Figure 7 shows the interface dynamics for several values of Δ toward the miscible limit $\Delta \rightarrow 0$, where the corresponding Weber number changes from $O(1)$ to $O(10^2)$; the initial states of the simulations are shown in Fig. 1(a). For $\Delta = 0.1$, Fig. 7(a) shows that the nonlinear growth of interface wave leads to the finger patterns and the fingers collapse to emit the quantized vortices at the stage of the shorter finger length than that shown in Fig. 3(a). This can be seen from the result of Fig. 4, where the elongation of the finger pattern is suppressed with decreasing Δ . Thus, we can say that the instability in this case is fairly in the macroscopic regime similar to that in Sec. IV.

A further decrease in Δ qualitatively changes the nonlinear dynamics. In Fig. 7(b) for $\Delta = 10^{-2}$ with $We \simeq 20$, the crossover between the obliquely striped density pattern [8] and the flutter-finger pattern, where the density modulation develops an array of multiple dipole-like structures consisting of pairs of density dips of each component along the overlapping region, as seen in the panels $\tilde{t} = 750$ and 815 of Fig. 7(b). Here, the density dip of the one component is filled with the density of the other component. These dipoles correspond to the pair of quantized vortices with the same circulation in each component. The array of the dipoles is subsequently collapsed by emitting the density wave into the bulk region, with irregular density patterns eventually appearing. Figure 7(c) for $\Delta = 10^{-3}$, satisfying $We \simeq 200$, clearly shows that the central overlapping region undergoes a characteristic modulation that leads to the obliquely striped density patterns [8]. These density stripes are subsequently collapsed from the central region ($\tilde{t} = 750$) and causes the turbulent structures ($\tilde{t} = 875$).

Note that the finger pattern of the Ψ_1 (Ψ_2) component in the universal macroscopic regime [Fig. 7(a)] grows in an upper-left (lower-right) direction, while the orientation of the stripe modulation in this case [Fig. 7(c)] is in the upper-right (lower-left) direction. The structure in Fig. 7(c) looks effectively to apply “friction” to the bulk flow, whereas the flutter-finger pattern seems to be parrying the flow as grass flutters in the wind. In fact, the CSI causes the frictional relaxation against the relative motion [33,34], which occurs more effectively when the two components overlap each other more and more. This is just like the function of ski skins attached to the bottom of nordic skis, designed to let the ski slide forward on snow but not backward by resembling sealskin. Here, the directions of the stripe and the bulk flow correspond to those of hairs on the sealskin and the motion of the ski, respectively. As seen in the profile of $\theta_1 = \arg\psi_1$ of Fig. 7(d), the interface layer in one component has a flow so as to penetrate into the other component and against its counterflow (see the panel $\tilde{t} = 650$). To distinguish the pattern formation in the early stage from the flutter-finger pattern we call this stripe pattern as the “sealskin pattern” in the diagram of Fig. 2.

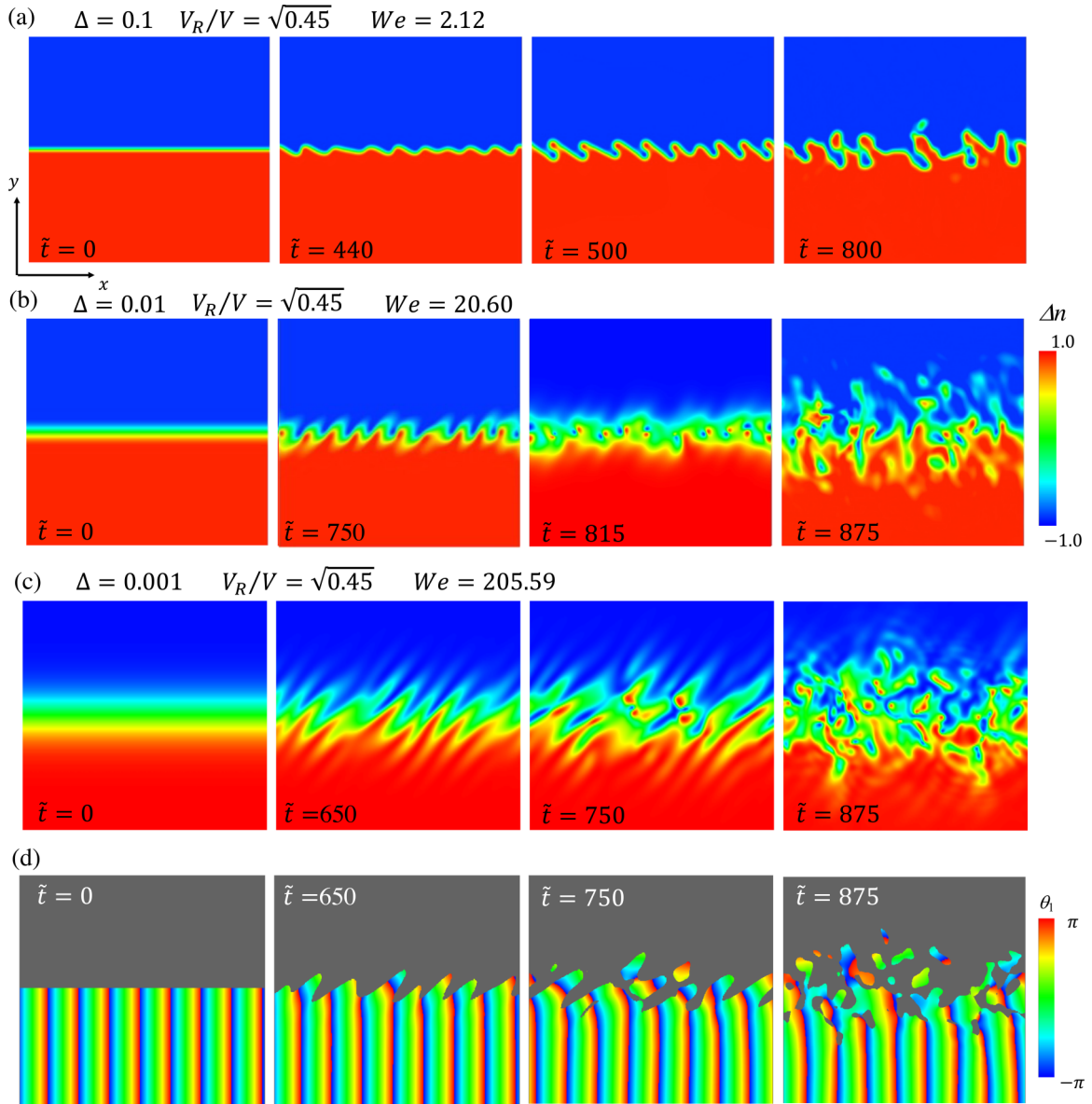


FIG. 7. Dynamics of the density difference Δn for $V_R/V = \sqrt{0.45}$ and (a) $\Delta = 10^{-1}$ ($We = 2.12$), (b) $\Delta = 10^{-2}$ ($We = 20.6$), and (c) $\Delta = 10^{-3}$ ($We = 205.6$). The red (blue) region corresponds to the area where the density n_1 (n_2) is located. In panel (d), the profile of the phase θ_1 corresponding to panel (c) is shown. The spatial region of the plot is $-150\xi \leq x, y \leq 150\xi$.

2. The results of the Bogoliubov-de Gennes analysis

For the CSI in a homogeneous system, the dynamical instability induces formation of a vortex–antivortex pair (in 2D) or a vortex ring (in 3D), which cause frictional relaxation of the countersuperflow due to the phase slip through a dissociation (expansion) of the vortex pair (vortex ring) [33,34]. In contrast, the friction in our case is caused by the penetration of the bulk flow along the oblique density stripe, like the sealskin. This qualitative difference can be clarified through the microscopic analysis based on the BdG equation.

Figure 8(a) shows the imaginary part of the BdG excitation spectrum as a function of k for the parameters corresponding to Fig. 7(c). The spectrum exhibits not only a main single branch but also an anomalously large number of unstable branches inside the main branch. From Fig. 8(a), the maxi-

imum of $\text{Im}[\omega]$ occurs at $k\xi = 0.218$, which determines the wavelength of the initially growing mode. However, the corresponding eigenfunction along the y direction also has a certain finite wave number, denoted k_y , as shown in Fig. 8(b). From the distribution of the real and imaginary parts of the eigenfunctions, the sign of k_y is negative. Also, note that the eigenfunctions satisfy the antisymmetric relation $\text{Re}[u_1(y)] = \text{Im}[v_2(-y)]$ and $\text{Im}[u_1(y)] = \text{Re}[v_2(-y)]$ in Fig. 8(b) (upper panel) and the similar relation in the Fig. 8(b) (lower panel). Thus, the norm of the excitations for each component $\mathcal{N}_j \equiv \int dy (|u_j|^2 - |v_j|^2)$ takes opposite sign. Since the Bogoliubov theory predicts that the current induced by the excitation is given by $\hbar k_y \mathcal{N}_j$ in the vertical direction, the eigenmode represents the counterpropagating excitations perpendicular to the interface. We find that $\mathcal{N}_1 < 0$ and $\mathcal{N}_2 > 0$ from Fig. 8(b) and the unstable mode results in the positive (negative) current for

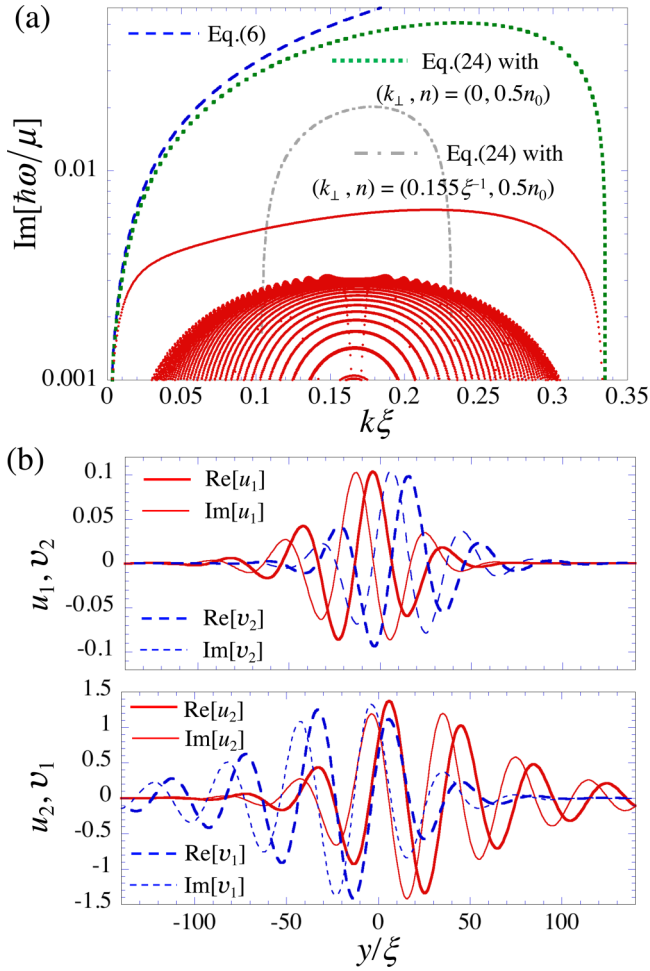


FIG. 8. (a) A semilog plot of $\text{Im}[\omega]$ of the dispersion relations for $V_R/V = \sqrt{0.45}$ and $\Delta = 0.001$. The numerical results obtained by the BdG equation are plotted by red points. The blue dashed curve represents the dispersion relation (6) of the KHI. Also, we plot $\text{Im}[\omega]$ obtained from the dispersion relation (24) of the CSI with $k_\perp = 0$ by the green dashed-dotted curve and $k_\perp = k_y^{\text{fit}}$ extracted from the eigenfunction in panel (b) by the gray dashed-dotted curve, where the fitting function $u^{\text{fit}} = |u_j|e^{ik_y^{\text{fit}}(y-y^{\text{fit}})}$ with the parameters k_y^{fit} and y^{fit} is employed; we here get $k_\perp\xi = 0.155$. In panels (b), we plot the eigenfunctions (u_1, v_1, u_2, v_2) corresponding to the largest value of $\text{Im}[\omega]$ in panel (a).

ψ_1 (ψ_2) component. These properties realize the excitation mode that induces the encroaching flow into the interface layer.

In Fig. 8(a), we compare the BdG results with the dispersion relations of the KH theory and the CSI in a homogeneous system. The dispersion relation Eq. (6) of the KHI is only coincident with the BdG result asymptotically at $k \rightarrow 0$, which implies the breakdown of KH theory. The appearance of the instability band may be explained as a signature of the CSI [33,34], where the CSI appears in some range of k_\parallel as well as the wave-number component k_\perp perpendicular to the direction of the counterflow. When we plot $\text{Im}[\omega]$ of Eq. (24) with $k_\perp = 0$, the unstable range of k agrees with the BdG results, although their magnitudes are quite different. The coincidence of the unstable range has been seen in Ref. [8].

Since the most unstable mode has a finite wave number in the y direction, as seen in Fig. 8(b), we also plot Eq. (24) with $k_\perp = 0.155$ extracted from the numerical fitting of the eigenfunction in Fig. 8(b). Then, the unstable range becomes narrow, which cannot reproduce the numerical result of the BdG result, and also the magnitude still overestimates the BdG result. Although the local approximation of the homogeneous CSI makes us expect the excitation modes having a momentum antiparallel to the initial condensate velocity leading the frictional relaxation, we also find that the excitation has nontrivially the momentum perpendicular to the interface to realize the obliquely encroaching flow. By using the BdG result, in fact, the oblique direction of the encroaching flow is explained by the BdG result as $\theta = \tan^{-1}(k_\parallel/k_\perp) = \tan^{-1} 1.406 = 0.3\pi$, reasonably in agreement with the GP result [see panel $\tilde{t} = 650$ of Fig. 7(c)]. These facts imply that the shear flow instability in the weakly segregating regime is qualitatively different from the homogeneous CSI; the difference could come from the fact that the density profile has a spatial gradient by the external potential in the former and Ref. [8] but not in the latter. To distinguish the homogeneous CSI with the CSI that causes sealskin pattern with a shear flow, we call the latter a sheared CSI.

VI. CONCLUSION AND DISCUSSION

In this work, we have studied detailed nonlinear dynamics of an interface in segregating two-component BECs with a shear flow by varying the intercomponent coupling strength and the relative velocity of the two components. The nonlinear dynamics induced by the KHI is characterized by the Weber number We , adopted to the segregated binary superfluids with the interface thickness l_d . The main result is summarized in the phase diagram of Fig. 2. For $We \lesssim 1$, the dynamics is characterized by a universal macroscopic behavior, which is relevant to the KHI in classical fluid dynamics. The dynamics induced by the KHI exhibit the formation of the flutter-finger pattern and its subsequent collapse by emitting the coreless quantized vortices at the tips of the fingers. These dynamical properties are characterized by the single parameter We ; we find that the growing finger length divided by l_d can be scaled as We^{-1} . For $We \gtrsim 1$, however, the nonlinear dynamics is caused by the microscopic mechanism beyond the conventional KHI and cannot be classified only by We . For $\Delta > 1$, a strongly segregated regime, the small-amplitude interface wave forms a transient zipper pattern. Since the vorticity per single wavelength is not enough to evolve into the vortex, the transition to the vortex turbulence configuration needs multiple steps of instability growth. In the weakly segregating regime $\Delta \ll 1$ with a large overlapping region, the instability gives rise to the frictional relaxation by forming a so-called sealskin pattern. We suggest the underlying mechanism of the sealskin pattern formation as the sheared CSI, which is qualitatively different from the homogeneous CSI.

Finally, let us discuss the crossover of the dynamical regime between the zipper and sealskin formation. As discussed above, the mechanism behind the sealskin pattern formation is partly the CSI around the overlapping region. Then, it is natural to compare the length scale of the overlapping region with the perturbation length. Since the

overlapping region vanishes when the interface thickness becomes thin, like $\approx \xi$, the overlapping length can be defined as $l_{\text{overlap}} = l_d - \xi$. The perturbation length can be estimated by the wave number that gives the maximum of $\text{Im}[\omega]$, which is approximately given by the dispersion relation of the homogeneous CSI. Since the characteristic wave number of the CSI is given by $k_{\text{CSI}} = mV_R/\hbar$ for a large V_R (see Appendix B), the curve $k_{\text{CSI}}l_{\text{overlap}} \approx 1$ could give a rough boundary between the zipper and sealskin region in the phase diagram of Fig. 2. The curve has a similar Δ dependence with We for the weakly segregating limit but exhibits a divergent behavior around $\Delta \approx 1$, where $l_d \approx \xi$. We confirm through GP simulations that the period and the amplitude of the sealskin pattern are decreased when the parameters are changed toward this curve from the $\Delta = 0.001$ and $V_R/V = \sqrt{0.45}$ [the parameters of Fig. 7(c)] and the zipper patterns begin to appear around the parameters on the boundary curve.

Since it is difficult to treat the extreme parameter values with $We \ll 1$ or $We \gg 1$ in numerical simulations, it should be noted that Fig. 2 represents the dynamical phase diagram of the crossover transition between the universal macroscopic regime and the microscopic regime. In outlook, more details in the latter regime remain to be studied. For example, we have to consider the finite-size effect of the CSI to account for the full behavior of the sheared CSI, seen in Figs. 6 and 8. Also, when the bulk velocity enters a supersonic regime, it is interesting to clarify the relation of the shock wave formation to the interface instability. Furthermore, it is necessary to consider the simulations under the realistic experimental setup in 3D, where the nonlinear stage of the time evolution causes the nucleation of vortex lines. These involve excitations of vortex waves, vortex reconnections, and subsequent formation of vortex rings and vortex tangles. These issues merit further studies and will be reported elsewhere.

ACKNOWLEDGMENTS

The work of K.K. was supported by KAKENHI Grant No. 18K03472 from the Japan Society for the Promotion of Science (JSPS) Grant-in-Aid for Scientific Research. H.T. was supported by JSPS KAKENHI Grants No. 18KK0391, No. JP20H01842, No. JP20H01843, and in part by the OCU ‘‘Think globally, act locally’’ Research Grant for Young Scientists through the hometown donation fund of Osaka City.

APPENDIX A: ANALOGY WITH ELECTROSTATICS IN STRONGLY SEGREGATED CONDENSATES WITH A SHEAR FLOW

In this Appendix, we describe an effective description of the strongly segregated condensates with a shear flow in Sec. IV A by introducing the analogy with electrostatics. This analogy is useful to understand qualitatively the vorticity distribution when the vortex sheet at the interface is deformed to the finger pattern.

In our setup, the first (second) component exists in the $y < 0$ ($y > 0$) region and the flat interface exists at $y = 0$, as shown in Fig. 9(a). The velocity of the each component is written as $\mathbf{v}_1 = (V_R/2, 0, 0)$ for $y < 0$ and $\mathbf{v}_2 = (-V_R/2, 0, 0)$ for $y > 0$. The mass current velocity $\mathbf{v} = (\rho_1\mathbf{v}_1 + \rho_2\mathbf{v}_2)/(\rho_1 + \rho_2)$ is

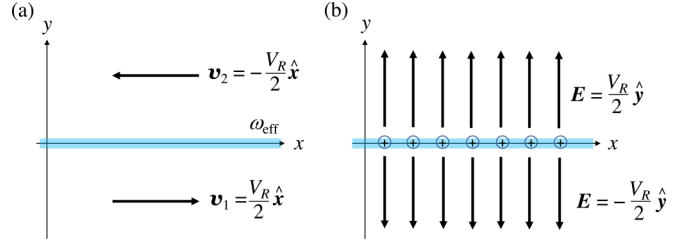


FIG. 9. The schematic illustration of our initial setup for the strongly segregating BECs with a shear flow. (a) The condensates are phase separated into $y < 0$ (ψ_1 component) and $y > 0$ (ψ_2 component) regions with the relative velocity V_R . The interface is located along the x axis, the vorticity being distributed in alignment with the x axis. (b) The electrostatic analogy of the configuration of panel (a). The vorticity corresponds to the positive charge, while the electric field is parallel to the contour lines of the phase θ_j .

given as

$$\mathbf{v} = \begin{cases} (+V_R/2, 0, 0) & \text{for } y < 0 \\ (-V_R/2, 0, 0) & \text{for } y > 0. \end{cases} \quad (\text{A1})$$

If the density is stationary, we can apply approximately the incompressible condition $\nabla \cdot \mathbf{v} = 0$, thereby defining the stream function ψ satisfying

$$v_x = \frac{\partial \psi}{\partial y}, \quad v_y = -\frac{\partial \psi}{\partial x}. \quad (\text{A2})$$

Then, the vorticity $\boldsymbol{\omega} = \nabla \times \mathbf{v} = (0, 0, \omega)$ can be expressed by the stream function as

$$\omega = -\nabla^2 \psi. \quad (\text{A3})$$

Since $\omega = 0$ in the region far from the interface, the stream function there obeys the Poisson equation

$$\nabla^2 \psi = 0. \quad (\text{A4})$$

Since \mathbf{v} is given by Eq. (A1) far from the interface, the solution of Eq. (A4) is written as

$$\psi = \begin{cases} \frac{V_R}{2}y & \text{for } y < 0 \\ -\frac{V_R}{2}y & \text{for } y > 0, \end{cases} \quad (\text{A5})$$

where we set $\psi = 0$ at $y = 0$.

According to the electrostatic analogy, the stream function ψ and the vorticity ω are related with the electrostatic potential and the charge density, respectively. The analog electric field \mathbf{E} is given by

$$\mathbf{E} = -\nabla \psi = \begin{cases} (0, -V_R/2, 0) & \text{for } y < 0 \\ (0, +V_R/2, 0) & \text{for } y > 0. \end{cases} \quad (\text{A6})$$

Thus, the situation is related to the electric field created by the uniformly distributed positive charge density ρ_e along the line $y = 0$, as shown in Fig. 9(b). By using Gauss’s law, we get $E = \rho_e/2$, where the dielectric constant is taken to be unity. Since the circulation along the sheet per unit length has the correspondence $\rho_\Gamma \leftrightarrow \rho_e$ we obtain the relation

$$\rho_\Gamma = V_R, \quad (\text{A7})$$

which is equivalent to Eq. (19).

The electrical flux lines exhibit a similar behavior with the branch cuts of the phase of the condensate wave function, as seen in Fig. 3. When the interface is deformed to the finger pattern, the vorticity, namely the positive charge, should be accumulated around the tips of the fingers, as seen in Fig. 3(c). This is because the electric field far from the interface is fixed by Eq. (A6), which gives the boundary condition to determine the charge distribution along the winding interface. As seen in the finger formation of the KHI dynamics, the strong deformation of the plane provides a cancellation of the electric field inside the domain of the fingers. Then, the charge density is more concentrated around the tips of the fingers. This charge distribution is actually observed in Figs. 3(b) and 3(c).

We confirm that the relation (A7) holds exactly by using the numerical solution of Eq. (2). In particular, for $\Delta = 2$ we can use the exact solution of Eq. (2) [43] to confirm this relation. The density profile of the strongly segregating BEC with $\Delta = 2$ is given by

$$\begin{aligned} |\phi_1| &= \frac{\sqrt{n_0}}{2} \left[1 - \tanh\left(\frac{y}{\sqrt{2}}\right) \right], \\ |\phi_2| &= \frac{\sqrt{n_0}}{2} \left[1 + \tanh\left(\frac{y}{\sqrt{2}}\right) \right]. \end{aligned} \quad (\text{A8})$$

According to the definition of \mathbf{v} , we have

$$v_x(y) = \frac{-V_R \tanh(y/\sqrt{2})}{1 + \tanh^2(y/\sqrt{2})}, \quad (\text{A9})$$

and the vorticity is

$$\omega(x, y) = \frac{V_R}{\sqrt{2}} \text{sech}^2(\sqrt{2}y). \quad (\text{A10})$$

Thus, the linear density of the vorticity is given by

$$\rho_\Gamma = \int dy \omega(x, y) = V_R, \quad (\text{A11})$$

which is consistent with the above discussion.

APPENDIX B: THE DISPERSION RELATION OF THE MISCIBLE BINARY BECS WITH COUNTERSUPERFLOW

We here describe briefly the derivation of the dispersion relation of the miscible two-component BECs with counterflow and show the dynamical instability known as the CSI [8,32–34]. The dispersion relation can be derived from the BdG analysis for a system of a uniform two-component BEC with a relative velocity. Starting from the time-dependent GP equations (1), we consider a small excitation $\delta\Psi_j$ above a uniform state with a velocity \mathbf{v}_j as

$$\Psi_j = (\sqrt{n_j} + \delta\Psi_j) e^{-i\mu_j t/\hbar + im_j \mathbf{v}_j \cdot \mathbf{r}/\hbar}, \quad (\text{B1})$$

where $\mu_j = g_j n_j + g_{j\bar{j}} n_{\bar{j}} + m_j v_j^2/2$ and $j, \bar{j} = 1, 2$ ($j \neq \bar{j}$). Although the miscibility condition $g_1 g_2 > g_{12}^2$ is generally supposed when the uniform solution $\sqrt{n_j}$ is employed, the dispersion relation is irrelevant to such a condition, which we do not assume here; the uniform solution itself is of course unstable for $g_1 g_2 < g_{12}^2$.

Substituting Eq. (B1) into Eq. (1) and taking the first order of $\delta\Psi_j$, we obtain ($j \neq \bar{j}$)

$$\begin{aligned} i\hbar \frac{\partial \delta\Psi_j}{\partial t} &= \left[-\frac{\hbar^2}{2m_j} \left(\nabla + i\frac{m\mathbf{v}_j}{\hbar} \right)^2 - \mu_j + 2g_j n_j \right. \\ &\quad \left. + g_{j\bar{j}} n_{\bar{j}} \right] \delta\Psi_j + g_j n_j \delta\Psi_j^* \\ &\quad + g_{j\bar{j}} \sqrt{n_j n_{\bar{j}}} (\delta\Psi_{\bar{j}} + \delta\Psi_{\bar{j}}^*). \end{aligned} \quad (\text{B2})$$

We expand the small excitation by the plane wave as

$$\delta\Psi_j = U_{j\mathbf{K}} e^{i\mathbf{K}\cdot\mathbf{r} - i\omega t} - V_{j\mathbf{K}}^* e^{-i\mathbf{K}\cdot\mathbf{r} + i\omega^* t}, \quad (\text{B3})$$

with the wave vector \mathbf{K} and the complex frequency ω , and substitute it into Eq. (B2), which yields ($j \neq j'$)

$$\left[\frac{\hbar^2}{2m_j} \left(K^2 + \frac{2m}{\hbar} \mathbf{K} \cdot \mathbf{v}_j \right) + g_j n_j \right] U_{j\mathbf{K}} - g_j n_j V_{j\mathbf{K}} + g_{j\bar{j}} \sqrt{n_j n_{\bar{j}}} (U_{\bar{j}\mathbf{K}} - V_{\bar{j}\mathbf{K}}) = \hbar\omega U_{j\mathbf{K}}, \quad (\text{B4a})$$

$$\left[\frac{\hbar^2}{2m_j} \left(K^2 - \frac{2m}{\hbar} \mathbf{K} \cdot \mathbf{v}_j \right) + g_j n_j \right] V_{j\mathbf{K}} - g_j n_j U_{j\mathbf{K}} - g_{j\bar{j}} \sqrt{n_j n_{\bar{j}}} (U_{\bar{j}\mathbf{K}} - V_{\bar{j}\mathbf{K}}) = -\hbar\omega V_{j\mathbf{K}}. \quad (\text{B4b})$$

Diagonalizing the eigenvalue equation (B4), we obtain the Bogoliubov excitation spectrum. Although the forms of the eigenvalues are generally complicated, the simplified form can be obtained by assuming $m_1 = m_2 \equiv m$, $g_1 = g_2 \equiv g$, and $n_1 = n_2 = n$. Then, the eigenvalue of Eq. (B4) becomes

$$\hbar\omega = \frac{\hbar}{2} (\mathbf{v}_1 + \mathbf{v}_2) \cdot \mathbf{K} \pm \sqrt{\varepsilon_0^2 + \varepsilon_r^2 + 2\varepsilon_0 g n \pm 2\sqrt{\varepsilon_0^2 \varepsilon_r^2 + 2\varepsilon_0 \varepsilon_r^2 g n + \varepsilon_0^2 g_{12}^2 n^2}}, \quad (\text{B5})$$

with $\varepsilon_0 = \hbar^2 K^2/(2m)$, $\varepsilon_r = \hbar k_{\parallel} V_R/2$, and the relative velocity $\mathbf{V}_R = \mathbf{v}_1 - \mathbf{v}_2$. Here, the wave number \mathbf{K} is decomposed to the components of the parallel and perpendicular directions as $\mathbf{K} = (k_{\parallel}, k_{\perp})$. The first term is neglected by assuming the situation of the vanishing center-of-mass velocity, namely, $\mathbf{v}_1 + \mathbf{v}_2 = 0$.

Figure 10 shows the imaginary part of Eq. (B5) in the $(k_{\parallel}, k_{\perp})$ plane for several values of V_R , representing the wave-number region associated with the dynamical instability. The unstable region appears inside the semicircle in the positive $(k_{\parallel}, k_{\perp})$ plane. The imaginary part of $\hbar\omega$ is finite when the expression

in the larger square root in Eq. (B5) with the negative sign becomes negative. The condition of the CSI is thus given by

$$\varepsilon_r^2 - 2(g + g_{12})n\varepsilon_0 < \varepsilon_0^2 < \varepsilon_r^2 - 2(g - g_{12})n\varepsilon_0. \quad (\text{B6})$$

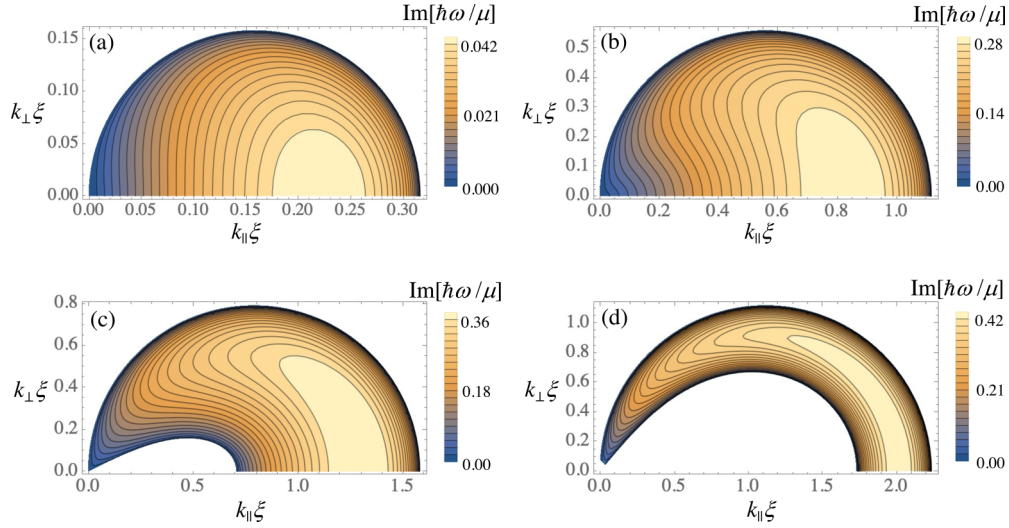


FIG. 10. The imaginary part of the eigenvalue of Eq. (B5) in the \mathbf{K} space for $g_{12} = g$, $n = n_0/2$, and several values of V_R : (a) $V_R = \sqrt{0.4}$, (b) $\sqrt{5}$, (c) $\sqrt{10}$, and (d) $\sqrt{20}$. The plot range is determined as $0 < k_{\parallel}\xi < V_R/(2V)$ and $0 < k_{\perp}\xi < V_R/(4V)$. The eigenvalue is scaled by $\mu = gn_0$.

At the miscible-immiscible boundary $g = g_{12}$, the right inequality of Eq. (B6) reduces to $(k_{\parallel} - mV_R/2\hbar)^2 + k_{\perp}^2 < (mV_R/2\hbar)^2$. As a result, the wave number of the unstable modes are characterized by $k_{\parallel} \lesssim mV_R/\hbar$ and $k_{\perp} \lesssim mV_R/2\hbar$.

With increasing V_R , the unstable modes are distributed in the higher- K region with a crescent shape, where the inner boundary of the crescent is determined by the left inequality of Eq. (B6).

-
- [1] M. Tsubota, M. Kobayashi, and H. Takeuchi, Quantum hydrodynamics, *Phys. Rep.* **522**, 191 (2013).
- [2] L. Kelvin, On the motion of free solids through a liquid, *Philos. Mag.* **42**, 362 (1871).
- [3] H. Helmholtz, On the discontinuous movements of fluids, *The London, Edinburgh, and Dublin Philos. Mag. J. Sci.* **36**, 337 (1868).
- [4] R. Blaauwgeers, V. B. Eltsov, G. Eska, A. P. Finne, R. P. Haley, M. Krusius, J. J. Ruohio, L. Skrbek, and G. E. Volovik, Shear Flow and Kelvin-Helmholtz Instability in Superfluids, *Phys. Rev. Lett.* **89**, 155301 (2002).
- [5] A. Finne, V. Eltsov, R. Hänninen, N. Kopnin, J. Kopu, M. Krusius, M. Tsubota, and G. Volovik, Dynamics of vortices and interfaces in superfluid ^3He , *Rep. Prog. Phys.* **69**, 3157 (2006).
- [6] V. B. Eltsov, A. Gordeev, and M. Krusius, Kelvin-Helmholtz instability of AB interface in superfluid ^3He , *Phys. Rev. B* **99**, 054104 (2019).
- [7] H. Takeuchi, N. Suzuki, K. Kasamatsu, H. Saito, and M. Tsubota, Quantum kelvin-Helmholtz instability in phase-separated two-component Bose-Einstein condensates, *Phys. Rev. B* **81**, 094517 (2010).
- [8] N. Suzuki, H. Takeuchi, K. Kasamatsu, M. Tsubota, and H. Saito, Crossover between Kelvin-Helmholtz and counter-superflow instabilities in two-component Bose-Einstein condensates, *Phys. Rev. A* **82**, 063604 (2010).
- [9] E. Lundh and J.-P. Martikainen, Kelvin-Helmholtz instability in two-component Bose gases on a lattice, *Phys. Rev. A* **85**, 023628 (2012).
- [10] A. W. Baggaley and N. G. Parker, Kelvin-Helmholtz instability in a single-component atomic superfluid, *Phys. Rev. A* **97**, 053608 (2018).
- [11] A. Mastrano and A. Melatos, Kelvin-Helmholtz instability and circulation transfer at an isotropic-anisotropic superfluid interface in a neutron star, *Mon. Not. R. Astron. Soc.* **361**, 927 (2005).
- [12] S. B. Papp, J. M. Pino, and C. E. Wieman, Tunable Miscibility in a Dual-Species Bose-Einstein Condensate, *Phys. Rev. Lett.* **101**, 040402 (2008).
- [13] G. Thalhammer, G. Barontini, L. De Sarlo, J. Catani, F. Minardi, and M. Inguscio, Double Species Bose-Einstein Condensate with Tunable Interspecies Interactions, *Phys. Rev. Lett.* **100**, 210402 (2008).
- [14] S. Tojo, Y. Taguchi, Y. Masuyama, T. Hayashi, H. Saito, and T. Hirano, Controlling phase separation of binary Bose-Einstein condensates via mixed-spin-channel Feshbach resonance, *Phys. Rev. A* **82**, 033609 (2010).
- [15] D. J. McCarron, H. W. Cho, D. L. Jenkin, M. P. Köppinger, and S. L. Cornish, Dual-species Bose-Einstein condensate of ^{87}Rb and ^{133}Cs , *Phys. Rev. A* **84**, 011603(R) (2011).
- [16] K. Sasaki, N. Suzuki, D. Akamatsu, and H. Saito, Rayleigh-Taylor instability and mushroom-pattern formation in a two-component Bose-Einstein condensate, *Phys. Rev. A* **80**, 063611 (2009).
- [17] S. Gautam and D. Angom, Rayleigh-Taylor instability in binary condensates, *Phys. Rev. A* **81**, 053616 (2010).
- [18] A. Bezett, V. Bychkov, E. Lundh, D. Kobayakov, and M. Marklund, Magnetic Richtmyer-Meshkov instability in a two-component Bose-Einstein condensate, *Phys. Rev. A* **82**, 043608 (2010).
- [19] K. Sasaki, N. Suzuki, and H. Saito, Dynamics of bubbles in a two-component Bose-Einstein condensate, *Phys. Rev. A* **83**, 033602 (2011).

- [20] D. Kobayakov, V. Bychkov, E. Lundh, A. Bezett, V. Akkerman, and M. Marklund, Interface dynamics of a two-component Bose-Einstein condensate driven by an external force, *Phys. Rev. A* **83**, 043623 (2011).
- [21] K. Sasaki, N. Suzuki, and H. Saito, Capillary instability in a two-component Bose-Einstein condensate, *Phys. Rev. A* **83**, 053606 (2011).
- [22] T. Kadokura, T. Aioi, K. Sasaki, T. Kishimoto, and H. Saito, Rayleigh-Taylor instability in a two-component Bose-Einstein condensate with rotational symmetry, *Phys. Rev. A* **85**, 013602 (2012).
- [23] T. Aioi, T. Kadokura, and H. Saito, Penetration of a vortex dipole across an interface of Bose-Einstein condensates, *Phys. Rev. A* **85**, 023618 (2012).
- [24] D. Kobayakov, A. Bezett, E. Lundh, M. Marklund, and V. Bychkov, Quantum swapping of immiscible Bose-Einstein condensates as an alternative to the Rayleigh-Taylor instability, *Phys. Rev. A* **85**, 013630 (2012).
- [25] D. Kobayakov, V. Bychkov, E. Lundh, A. Bezett, and M. Marklund, Parametric resonance of capillary waves at the interface between two immiscible Bose-Einstein condensates, *Phys. Rev. A* **86**, 023614 (2012).
- [26] F. Tsitoura, V. Achilleos, B. A. Malomed, D. Yan, P. G. Kevrekidis, and D. J. Frantzeskakis, Matter-wave solitons in the counterflow of two immiscible superfluids, *Phys. Rev. A* **87**, 063624 (2013).
- [27] S. Hayashi, M. Tsubota, and H. Takeuchi, Instability crossover of helical shear flow in segregated Bose-Einstein condensates, *Phys. Rev. A* **87**, 063628 (2013).
- [28] V. A. Brazhnyi, D. Novoa, and C. P. Jisha, Dynamical generation of interwoven soliton trains by nonlinear emission in binary Bose-Einstein condensates, *Phys. Rev. A* **88**, 013629 (2013).
- [29] D. Kobayakov, A. Bezett, E. Lundh, M. Marklund, and V. Bychkov, Turbulence in binary Bose-Einstein condensates generated by highly nonlinear Rayleigh-Taylor and Kelvin-Helmholtz instabilities, *Phys. Rev. A* **89**, 013631 (2014).
- [30] H. Takeuchi, Domain-area distribution anomaly in segregating multicomponent superfluids, *Phys. Rev. A* **97**, 013617 (2018).
- [31] K.-T. Xi, T. Byrnes, and H. Saito, Fingering instabilities and pattern formation in a two-component dipolar Bose-Einstein condensate, *Phys. Rev. A* **97**, 023625 (2018).
- [32] C. K. Law, C. M. Chan, P. T. Leung, and M.-C. Chu, Critical velocity in a binary mixture of moving Bose condensates, *Phys. Rev. A* **63**, 063612 (2001).
- [33] H. Takeuchi, S. Ishino, and M. Tsubota, Binary Quantum Turbulence Arising from Countersuperflow Instability in Two-Component Bose-Einstein Condensates, *Phys. Rev. Lett.* **105**, 205301 (2010).
- [34] S. Ishino, M. Tsubota, and H. Takeuchi, Countersuperflow instability in miscible two-component Bose-Einstein condensates, *Phys. Rev. A* **83**, 063602 (2011).
- [35] C. Hamner, J. J. Chang, P. Engels, and M. A. Hoefer, Generation of Dark-Bright Soliton Trains in Superfluid-Superfluid Counterflow, *Phys. Rev. Lett.* **106**, 065302 (2011).
- [36] M. A. Hoefer, J. J. Chang, C. Hamner, and P. Engels, Dark-dark solitons and modulational instability in miscible two-component Bose-Einstein condensates, *Phys. Rev. A* **84**, 041605(R) (2011).
- [37] J. H. Kim, S. W. Seo, and Y. Shin, Critical Spin Superflow in a Spinor Bose-Einstein Condensate, *Phys. Rev. Lett.* **119**, 185302 (2017).
- [38] C. J. Pethick and H. Smith, *Bose-Einstein Condensation in Dilute Gases* (Cambridge University Press, Cambridge, 2008).
- [39] E. Timmermans, Phase Separation of Bose-Einstein Condensates, *Phys. Rev. Lett.* **81**, 5718 (1998).
- [40] P. Ao and S. T. Chui, Binary Bose-Einstein condensate mixtures in weakly and strongly segregated phases, *Phys. Rev. A* **58**, 4836 (1998).
- [41] G. E. Volovik, On the Kelvin-Helmholtz instability in superfluids, *JETP Lett.* **75**, 418 (2002).
- [42] B. Van Schaeybroeck, Interface tension of Bose-Einstein condensates, *Phys. Rev. A* **78**, 023624 (2008).
- [43] J. O. Indekeu, C.-Y. Lin, N. Van Thu, B. Van Schaeybroeck, and T. H. Phat, Static interfacial properties of Bose-Einstein condensate mixtures, *Phys. Rev. A* **91**, 033615 (2015).
- [44] R. A. Barankov, Boundary of two mixed Bose-Einstein condensates, *Phys. Rev. A* **66**, 013612 (2002).
- [45] A. T. Dinh, H. O. Haraldsson, Z. L. Yang, and B. R. Sehgal, Simulation of viscous stabilization of Kelvin-Helmholtz instability, *WIT Trans. Eng. Sci.* **29**, 425 (2000).
- [46] T. Atmakidis and E. Y. Kenig, A study on the Kelvin-Helmholtz instability using two different computational fluid dynamics methods, *J. Comput. Multiph. Flows* **2**, 33 (2010).
- [47] See Supplemental Material at <http://link.aps.org/supplemental/10.1103/PhysRevA.104.023312> for videos of the dynamics.
- [48] K. Kasamatsu, M. Tsubota, and M. Ueda, Vortices in multi-component Bose-Einstein condensates, *Int. J. Mod. Phys. B* **19**, 1835 (2005).
- [49] A. Richaud, V. Penna, R. Mayol, and M. Guilleumas, Vortices with massive cores in a binary mixture of Bose-Einstein condensates, *Phys. Rev. A* **101**, 013630 (2020).
- [50] K. Kasamatsu, M. Tsubota, and M. Ueda, Spin textures in rotating two-component Bose-Einstein condensates, *Phys. Rev. A* **71**, 043611 (2005).
- [51] R. P. Feynman, R. B. Leighton, and M. L. Sands, *The Feynman Lectures on Physics: Electromagnetism and Matter* (Addison-Wesley Publishing Company, Boston, 1964), Vol. 2.
- [52] G. A. El, A. Gammal, and A. M. Kamchatnov, Oblique Dark Solitons in Supersonic Flow of a Bose-Einstein Condensate, *Phys. Rev. Lett.* **97**, 180405 (2006).
- [53] I. Carusotto, S. X. Hu, L. A. Collins, and A. Smerzi, Bogoliubov-Čerenkov Radiation in a Bose-Einstein Condensate Flowing Against an Obstacle, *Phys. Rev. Lett.* **97**, 260403 (2006).
- [54] R. G. Scott and D. A. W. Hutchinson, Incoherence of Bose-Einstein condensates at supersonic speeds due to quantum noise, *Phys. Rev. A* **78**, 063614 (2008).
- [55] T.-L. Horng, S.-C. Gou, T.-C. Lin, G. A. El, A. P. Itin, and A. M. Kamchatnov, Stationary wave patterns generated by an impurity moving with supersonic velocity through a Bose-Einstein condensate, *Phys. Rev. A* **79**, 053619 (2009).